THE ASTROPHYSICAL JOURNAL, 562:208–232, 2001 November 20

PARSEC-SCALE JET POLARIZATION PROPERTIES OF A COMPLETE SAMPLE OF ACTIVE GALACTIC NUCLEI AT 43 GHz

MATTHEW L. LISTER[1]
National Radio Astronomy Observatory, 520 Edgemont Road, Charlottesville, VA 22903-2454; mlister@nrao.edu
Received 2001 March 13; accepted 2001 July 27

ABSTRACT

We present results from the highest resolution polarization imaging survey of a complete sample of extragalactic radio sources carried out to date. Our sample consists of a statistically complete flat-spectrum subset of 32 active galactic nuclei (AGNs) from the Pearson-Readhead survey, which has been studied at a variety of wavelengths and resolutions, including space-VLBI. Our observations were made with the VLBA at 43 GHz, at which the relatively higher resolution and weaker opacity effects have allowed us to probe magnetic field structures in the jets of these AGNs much closer to the central engine than in previous studies. At 43 GHz, the bulk of the total intensity and polarized emission in most flat-spectrum AGNs originates from an unresolved core component located at the extreme end of a faint jet. The luminosity of the core is positively correlated with the total source luminosity in soft X-rays, in the optical, and at 5 GHz. The most strongly polarized cores display electric vectors that are preferentially aligned with the jet axis, which is consistent with a strong transverse shock that enhances the perpendicular component of the jet magnetic field. Sources with highly polarized cores also tend to have high optical polarizations and flatter overall radio spectra. Approximately half of the AGNs in our sample display apparently bent jet morphologies that are suggestive of streaming motions along a helical path. The straightest jets in the sample tend to display slower superluminal speeds than those that are significantly bent. Our observations also show that intrinsic differences in the jet magnetic field properties of BL Lac objects and quasars previously seen on scales of tens of milliarcseconds are also present in regions much closer to the base of the jet.

Subject headings: BL Lacertae objects: general — galaxies: active — galaxies: jets — polarization — quasars: general — radio continuum: galaxies

1. INTRODUCTION

Studies of active galactic nuclei (AGNs) with polarization-sensitive VLBI currently provide us with one of the best means of investigating the magnetic field structures of outflows from the vicinity of supermassive black holes. Theoretical and numerical simulations of these outflows suggest that they are highly collimated and accelerated to relativistic speeds by magnetic fields generated in a rapidly rotating accretion disk (see the recent review by Meier, Koide, & Uchida 2001). Many of these outflows are believed to undergo strong shocks that significantly alter their observed polarization structure (e.g., Hughes, Aller, & Aller 1985).

Past VLBI polarization observations of large AGN samples (e.g., Cawthorne et al. 1993; Gabuzda, Pushkarev, & Cawthorne 2000) have led to important discoveries regarding relativistic shocks and the underlying magnetic fields of AGN jets. These surveys have generally been carried out at cm wavelengths, however, at which Faraday effects can be important. At shorter observing wavelengths, it is possible to probe regions much closer to the base of the jet because of the λ^{-1} improvement in angular resolution and lower source opacities. The higher resolution afforded at mm wavelengths is especially important in alleviating the effects of blending within the synthesized beam, which can dramatically reduce the observed polarized emission from closely spaced, orthogonally polarized regions. Faraday rotation and depolarization effects are also greatly diminished in the mm regime, enabling a more accurate determination of true magnetic field directions.

We present here the results of the first VLBI polarization study of a complete sample of flat-spectrum AGNs at a wavelength of $\lambda = 7$ mm ($\nu = 43$ GHz). The synthesized beam in our images has a typical FWHM angular size of ~ 0.2 mas, making this the highest resolution imaging survey of a complete AGN sample made to date. Our sample is drawn from the well-known Pearson-Readhead (PR) survey (Pearson & Readhead 1988), which has been the subject of numerous studies at a variety of wavelengths and resolutions, including space-VLBI at 5 GHz (Lister et al. 2001a). The latter data have allowed us to trace weak, steep-spectrum jet emission out to much larger distances from the core than is possible at 43 GHz alone.

The paper is laid out as follows. In § 2 we describe our sample selection criteria, followed by a discussion of our observations and data analysis methods in § 3. In § 4 we discuss various correlations between observed properties of our sample and their implications for current jet and shock models. These include correlations involving VLBI core-component luminosity and polarization, and the morphology and polarization properties of components located farther down the jet. We also discuss a correlation between the apparent bending morphologies and speeds in AGN jets and demonstrate how many of the bent jet morphologies in our sample are consistent with low-pitch helical jet trajectories. In § 5 we discuss apparent differences in the intrinsic magnetic field structures of BL Lac objects and quasars at 43 GHz that support previous findings at lower observing frequencies. We summarize our results in § 6.

Throughout this paper we use a Freidmann cosmology, with $H_0 = 100\,h$ km s^{-1} Mpc^{-1}, $h = 0.65$, $q_0 = 0.1$, and a zero cosmological constant. We give all position angles in

[1] Former address: Jet Propulsion Laboratory, California Institute of Technology, MS 238-332, 4800 Oak Grove Drive, Pasadena, CA 91109.

degrees east of north, and define the spectral index according to $S_\nu \propto \nu^\alpha$. All fractional polarizations are quoted in percents and refer to linear polarization only.

2. SAMPLE SELECTION

Our sample is derived from the PR survey (Pearson & Readhead 1988), which consists of all northern ($\delta > +35°$) AGNs with total 5 GHz flux density greater than 1.3 Jy and galactic latitude $|b| > 10°$. Since the steep-spectrum lobe emission can still make a significant contribution to the total flux of an AGN at 5 GHz, many of the arcsecond-scale core components in the PR sample are extremely radio weak ($\lesssim$1 mJy at 43 GHz). In order to select a statistically complete core-selected sample that is suitable for snapshot imaging with the NRAO's[2] Very Long Baseline Array (VLBA), we used a spectral-flatness criterion $\bar{\alpha}_{5-15} > -0.4$, where $\bar{\alpha}_{5-15}$ is a time-averaged single-dish spectral index between 5 and 15 GHz measured by Aller, Aller, & Hughes (1992). This final flat-spectrum Pearson-Readhead (FS-PR) sample was originally defined in a related paper (Lister, Tingay, & Preston 2001b) and contains 21 quasars, nine BL Lac objects, and two radio galaxies (see Table 1).

[2] The National Radio Astronomy Observatory is a facility of the National Science Foundation operated under cooperative agreement by Associated Universities, Inc.

TABLE 1

GENERAL PROPERTIES OF PEARSON-READHEAD AGNs

IAU Name (1)	Other Name (2)	Optical Class (3)	z (4)	log L_{tot} (W Hz^{-1}) (5)	m_{tot} (%) (6)	m_{opt} (%) (7)	JPA (deg) (8)	N_{bend} (9)	Σ_{bend} (deg) (10)	Bend & Realign (11)
Flat-Spectrum (FS-PR) Sample Objects										
0016+731.....	...	Q	1.781	27.78	2.2	0.9	132	2	66	N
0133+476.....	OC 457	HPQ	0.859	27.95	5.3	20.8	330	0	0	N
0212+735.....	...	HPQ	2.367	28.56	4.9	0.7	121	4	159	Y
0316+413.....	3C 84	RG	0.017	24.52	<0.1	0.6	176	0	0	N
0454+844.....	...	BL	0.112	24.54	<2.4	14.2	177	0	0	Y
0723+679.....	3C 179	LPRQ	0.844	27.12	1.3	1.0	256	1	24	N
0804+499.....	OJ 508	HPQ	1.432	27.59	1.3	8.6	127	1	11	N
0814+425.....	OJ 425	BL	0.245	26.13	3.7	8.7	103	2	142	Y
0836+710.....	4C 71.07	Q	2.180	28.38	1.7	1.0	201	3	45	Y
0850+581.....	4C 58.17	LPRQ	1.322	27.21	<1.6	0.4	227	4	147	Y
0859+470.....	4C 47.29	Q	1.462	27.46	2.6	0.7	357	2	43	N
0906+430.....	3C 216	HPQ	0.670	26.81	1.7	3.8	151	0	0	Y
0923+392.....	4C 39.25	LPRQ	0.699	28.11	5.6	0.4	93	2	59	Y
0945+408.....	4C 40.24	LPRQ	1.252	27.86	4.2	0.3	137	4	65	Y
0954+556.....	4C 55.17	HPQ	0.900	...	...	6.4	191	1	106	N
0954+658.....	...	BL	0.367	26.19	1.0	6.4	311	1	41	N
1624+416.....	4C 41.32	Q	2.550	28.00	1.2	...	262	2	193	N
1633+382.....	4C 38.41	HPQ	1.807	28.40	2.9	1.1	279	5	194	N
1637+574.....	OS 562	Q	0.749	27.55	5.5	2.4	200	0	0	Y
1641+399.....	3C 345	HPQ	0.595	27.90	5.3	11.2	284	4	203	Y
1642+690.....	4C 69.21	HPQ	0.751	27.31	5.8	16.6	158	3	109	Y
1652+398.....	MK 501	BL	0.033	24.10	1.5	3.0	160	3	225	Y
1739+522.....	4C 51.37	HPQ	1.381	27.65	1.9	3.7	204	2	185	N
1749+701.....	...	BL	0.770	26.82	<0.6	10.5	275	3	248	N
1803+784.....	...	BL	0.680	27.40	8.7	7.0	291	1	25	N
1807+698.....	3C 371	BL	0.050	24.68	<0.5	8.0	252	1	10	N
1823+568.....	4C 56.27	BL	0.663	27.24	8.4	16.8	201	2	40	Y
1928+738.....	4C 73.18	LPRQ	0.302	26.83	3.1	1.2	166	3	164	Y
1954+513.....	OV 591	Q	1.223	27.67	3.2	1.2	307	0	0	Y
2021+614.....	OW 637	RG	0.228	26.21	<0.3	0.3	214	0	0	N
2200+420.....	BL Lac	BL	0.069	25.81	4.0	13.7	209	1	65	N
2351+456.....	4C 45.51	Q	1.986	28.21	1.8	...	321	1	19	N
Other PR Sample Objects										
0153+744.....	...	Q	2.338	27.12	<2.3	1.1	68	2	151	N
0538+498.....	3C 147	LPRQ	0.545	26.39	<1.9	2.3	237	0	0	N
0711+356.....	OI 318	Q	1.620	27.08	<1.6	1.0	329	0	0	N
1828+487.....	3C 380	LPRQ	0.692	27.27	3.8	0.2	311	4	143	Y

NOTE.—All quantities are derived assuming $h = 0.65$, $q_0 = 0.1$, and a zero cosmological constant. Col. (1): IAU source name. Col. (2): Alternate name. Col. (3): Optical classification: RG: radio galaxy; BL: BL Lac object; HPQ: high (optical) polarization radio quasar; LPRQ: low (optical) polarization radio quasar; Q: radio quasar with unknown optical polarization. Col. (4): Redshift from Lawrence et al. (1996). Col. (5): Total VLBI luminosity at 43 GHz. Col. (6): Total VLBI integrated fractional polarization of source at 43 GHz. Col. (7): Total optical fractional polarization of source. Col. (8): Innermost JPA on parsec scales. Col. (9): Number of significant jet bends (greater than 10°) within 100 h^{-1} projected pc of the core. Col. (10): Sum of significant bend angles within 100 h^{-1} projected pc of the core. Col. (11): Jet bend and realign (BAR) morphology (see § 4.7.2).

3. OBSERVATIONS AND DATA ANALYSIS

We obtained single-epoch 43 GHz VLBA polarization data on the entire FS-PR sample with the exception of 0954+556. This unusual flat-spectrum object has a weak core at high frequencies and an apparent compact symmetric morphology (e.g., Wilkinson et al. 1994) at 8.4 GHz (A. P. Marscher 2000, private communication). We also observed four PR sources that did not satisfy the flat-spectrum cutoff: 0153+744, 0538+498, 0711+356, and 1828+487. We include their images and data here, but do not consider them in the statistical analyses that follow. We carried out observations of 28 sources over three separate VLBA sessions, with approximately 60 minutes integration time devoted to each source. During the first observing session (1999 April 6), only right-hand circular polarization data were obtained at Owens Valley because of a receiver failure. No data were obtained with the Brewster antenna during the 2000 September 10 session, also because of a receiver failure. Data from all ten VLBA antennas were obtained during the 2000 January 3 session.

The data were recorded in eight baseband channels (intermediate frequencies: IFs) of 8 MHz bandwidth using 1-bit sampling. Both right- and left-hand polarizations were recorded simultaneously in IF pairs, giving a total observing bandwidth of 32 MHz. Snapshot data on seven remaining FS-PR sources were made available to us from other VLBA programs that used identical observing parameters (see Table 2).

The data were correlated using the VLBA correlator in Socorro, NM, and subsequent data editing and calibration were performed at the Jet Propulsion Laboratory using the Astronomical Image Processing System (AIPS) software supplied by NRAO. Our calibration method followed that of Lister & Smith (2000). For each observing session, we determined the antenna polarization leakage factors by running the AIPS task LPCAL on four program sources and averaging the resulting solutions. The antenna leakage factors ranged from approximately 1% to 7% and had a typical scatter of 0.7%. Based on 37 GHz flux-density measurements of 1803+794 from the Metsähovi observatory (H. Teräsranta 2000, private communication), we estimate our absolute flux-density scaling to be accurate to within $\sim$20%.

We determined the absolute electric vector position angle (EVPA) corrections using measurements of component C4 in 3C 279 at each observing epoch (see Taylor 2000). As an additional check on our calibration, we found good agreement between our integrated EVPA for our 2000 September 10 epoch of 3C 279 and the measured value from the NRAO's Very Large Array (VLA)[3] on the following day. Based on these comparisons, we estimate that our measured EVPAs are accurate to within $\sim 5^\circ$.

We used the Caltech DIFMAP package (Pearson et al. 1994) to make Stokes I, Q, and U images of our sources, which we then imported into AIPS to make our final contour images, shown in Figures 1–32. The images of 0923+392, 1633+382, and 1928+738 are presented in Lister & Smith (2000). In the interest of completeness, we include unpublished images of 1652+398 from A. P. Marscher (2000, private communication) and those of 1641+399, 1823+487, and 2200+420 from S. G. Jorstad (in preparation). The parameters for all of the images are summarized in Table 2.

[3] See Web site http://www.aoc.nrao.edu/~smyers/calibration/.

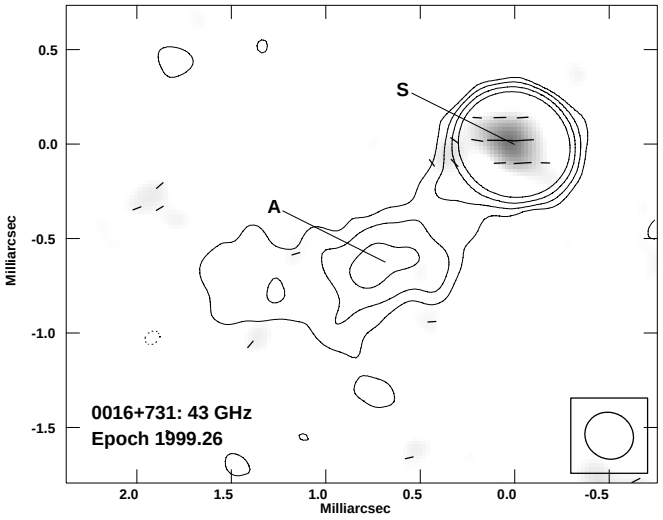

FIG. 1.—VLBA total intensity image of 0016+731 at 43 GHz, with electric vectors superimposed. The gray scale indicates linearly polarized intensity.

We performed elliptical Gaussian model fits to each source in the (u, v) plane using the task MODELFIT in DIFMAP. In cases in which elliptical Gaussians provided a poor fit to the visibilities, we used point (δ-function) components. The results of these fits are given in Tables 3 and 4 and are intended as a general guideline for interpreting the source structure. We estimate the given positions of strong, isolated components to be accurate to within a quarter of a beam width, and their measured flux densities to be accurate to within $\lesssim$10%. Our fits are less reliable for weak components and those located in regions of diffuse emission.

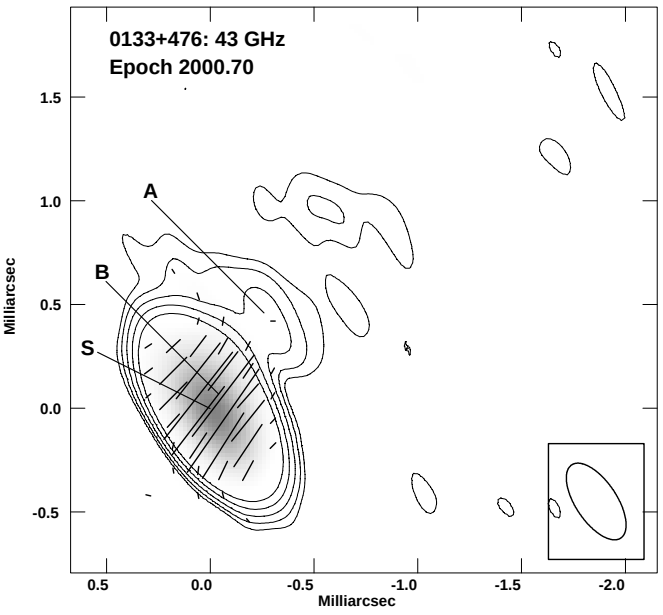

FIG. 2.—VLBA total intensity image of 0133+476 (OC 457) at 43 GHz, with electric vectors superimposed. The gray scale indicates linearly polarized intensity.

TABLE 2

SUMMARY OF 43 GHz IMAGE PARAMETERS

Source (1)	Observation Date (2)	Type (3)	Beam (mas) (4)	P.A. (deg) (5)	Flux (mJy) (6)	EV (mJy mas $^{-1}$) (7)	Dynamic Range (peak/rms) (8)	Peak (mJy beam $^{-1}$) (9)	Contour Levels (10)
0016+731	1999 Apr 6	IPOL	0.26 × 0.24	58	668	...	1.0	598	−0.4, 0.4, 0.8, 1.6, 3.2
		PPOL	...	...	15	88	0.8	12	...
0133+476	2000 Sep 10	IPOL	0.32 × 0.20	34	4464	...	2.1	4049	−0.125, 0.125, 0.25, 0.5, 1, 2
		PPOL	...	...	238	306	1.1	198	...
0153+744	2000 Jan 5	IPOL	0.29 × 0.26	−85	87	...	0.6	81	−1.75, 1.75, 3.5, 7, 14, 28, 56
		PPOL	...	...	<2.0	35	0.4	3.4	...
0212+735	1999 Apr 6	IPOL	0.22 × 0.19	63	1226	...	1.7	451	−1, 1, 2, 4, 8, 16, 32, 64
		PPOL	...	...	60	117	1.1	25	...
0316+413	1999 Apr 6	IPOL	0.30 × 0.20	−7	4362	...	2.9	973	−1.1, 1.1, 2.2, 4.4, 8.8, 17.6, 35.2, 70.4
		PPOL	...	...	<5.5	47	1.1	7.0	...
0454+844	2000 Jan 5	IPOL	0.34 × 0.31	−19	106	...	0.5	81	−1.75, 1.75, 3.5, 7, 14, 28, 56
		PPOL	...	...	<2.5	35	0.5	2.7	...
0538+498	1999 Apr 6	IPOL	0.28 × 0.22	−8	286	...	1.4	172	−2.25, 2.25, 4.5, 9, 18, 36, 72
		PPOL	...	...	<5.5	70	1.1	7.7	...
0711+356	2000 Jan 5	IPOL	0.40 × 0.23	−17	122	...	0.6	71	−2, 2, 4, 8, 16, 32, 64
		PPOL	...	...	<2.0	18	0.4	3.5	...
0723+679	2000 Sep 10	IPOL	0.39 × 0.20	90	712	...	1.1	637	−0.4, 0.4, 0.8, 1.6, 3.2, 6.4, 12.8, 25.6
		PPOL	...	...	9.5	61	0.9	13	...
0804+499	1999 Apr 6	IPOL	0.29 × 0.20	−29	721	...	0.7	697	−0.3, 0.3, 0.6, 1.2, 2.4, 4.8, 9.6
		PPOL	...	...	9.5	78	0.8	11	...
0814+425	2000 Jan 5	IPOL	0.31 × 0.24	0	862	...	0.7	724	−0.25, 0.25, 0.5, 1, 2, 4, 8
		PPOL	...	...	32	47	0.6	27	...
0836+710	1999 Apr 6	IPOL	0.25 × 0.23	−53	1434	...	1.1	1091	−0.3, 0.3, 0.6, 1.2, 2.4, 4.8, 9.6, 19.2, 38.4, 76.8
		PPOL	...	...	24	70	0.7	17	...
0850+581	2000 Sep 10	IPOL	0.45 × 0.21	−81	278	...	1.7	206	−1.5, 1.5, 3, 6, 12
		PPOL	...	...	<4.5	31	0.9	5.0	...
0859+470	2000 Jan 5	IPOL	0.37 × 0.26	−2	389	...	0.6	253	−0.75, 0.75, 1.5, 3, 6, 9, 18, 36
		PPOL	...	...	10	18	0.4	8.5	...
0906+430	1999 Apr 6	IPOL	0.41 × 0.38	−85	498	...	0.9	375	−0.75, 0.75, 1.5, 3, 6, 9, 18, 36, 72
		PPOL	...	...	8.5	35	0.5	10	...
0923+392[a]	1999 Jan 12	IPOL	0.29 × 0.17	−1	6986	...	1.3	2204	−0.4, 0.4, 0.8, 1.6, 3.2, 6.4, 12.8, 25.6, 51.2
		PPOL	...	...	394	233	1.5	160	...
0945+408	2000 Jan 5	IPOL	0.24 × 0.17	0	1176	...	1.4	670	−0.6, 0.6, 1.2, 2.4, 4.8, 9.6, 19.2, 38.4
		PPOL	...	...	49	140	1.1	36	...
0954+658	1999 Apr 6	IPOL	0.25 × 0.21	−74	448	...	0.9	402	−0.7, 0.7, 1.4, 2.8, 5.6, 11.2, 22.4
		PPOL	...	...	4.5	47	0.9	6.9	...
1624+416	1999 Apr 6	IPOL	0.38 × 0.27	−17	339	...	1.0	227	−0.65, 0.65, 1.3, 2.6, 5.2, 10.4, 20.8
		PPOL	...	...	4.1	35	1.0	7.0	...
1633+382[a]	1999 Jan 12	IPOL	0.33 × 0.21	−13	2286	...	0.7	1736	−0.125, 0.125, 0.25, 0.5, 1, 2, 4, 8, 16, 95
		PPOL	...	...	67	156	0.9	43	...
1637+574	1999 Apr 6	IPOL	0.26 × 0.22	4	1898	...	0.7	1019	−0.15, 0.15, 0.3, 0.6, 1.2, 2.4, 4.8, 57.6
		PPOL	...	...	104	88	0.7	42	...
1641+399	1998 Jul 31	IPOL	0.24 × 0.17	−16	8168	...	1.8	4887	−0.15, 0.15, 0.3, 0.6, 1.2, 2.4, 4.8, 9.6
		PPOL	...	...	433	205	1.2	252	...
1642+690	2000 Sep 10	IPOL	0.25 × 0.21	−30	1232	...	0.7	1061	−0.2, 0.2, 0.4, 0.8, 1.6, 3.2
		PPOL	...	...	72	77	0.5	65	...

TABLE 2—*Continued*

Source (1)	Observation Date (2)	Type (3)	Beam (mas) (4)	P.A. (deg) (5)	Flux (mJy) (6)	EV (mJy mas $^{-1}$) (7)	Dynamic Range (peak/rms) (8)	Peak (mJy beam $^{-1}$) (9)	Contour Levels (10)
1652+398	1997 May 26	IPOL	0.35 × 0.22	−9	461	...	0.6	231	−0.7, 0.7, 1.4, 2.8, 5.6
		PPOL	...	...	6.7	17	0.6	6.7	...
1739+522	2000 Sep 10	IPOL	0.30 × 0.20	−19	782	...	0.7	657	−0.25, 0.25, 0.5, 1, 2
		PPOL	...	...	15	57	0.5	16	...
1749+701	2000 Sep 10	IPOL	0.27 × 0.21	−29	354	...	0.7	197	−0.9, 0.9, 1.8, 3.6, 7.2, 14.4, 28.8, 57.6, 95
		PPOL	...	...	<2.0	20	0.5	4.0	...
1803+784	1999 Apr 6	IPOL	0.20 × 0.17	39	1863	...	1.4	1165	−0.4, 0.4, 0.8, 1.6, 3.2, 6.4, 12.8, 25.6
		PPOL	...	...	162	350	1.0	71	...
1807+698	1999 Apr 6	IPOL	0.29 × 0.24	63	735	...	0.8	381	−0.6, 0.6, 1.2, 2.4, 4.8, 9.6, 19.2, 38.4, 76.8
		PPOL	...	...	<4.0	700	0.8	5.0	...
1823+568	1998 Jul 31	IPOL	0.23 × 0.17	−21	1413	...	0.9	1057	−0.3, 0.3, 0.6, 1.2, 2.4, 4.8
		PPOL	...	...	119	123	1.0	90	...
1828+487	2000 Sep 10	IPOL	0.33 × 0.23	−5	1230	...	0.7	808	−0.25, 0.25, 0.5, 1, 2, 4
		PPOL	...	...	47	31	0.5	22	...
1928+738[a]	1999 Jan 12	IPOL	0.27 × 0.25	54	2423	...	0.8	1284	−0.25, 0.25, 0.5, 1, 2, 4, 8, 16, 32, 64
		PPOL	...	...	76	156	0.8	37	...
1954+513	1999 Apr 6	IPOL	0.27 × 0.23	−10	1005	...	0.8	780	−0.3, 0.3, 0.6, 1.2, 2.4, 4.8, 9.6, 19.2
		PPOL	...	...	32	70	0.8	32	...
2021+614	1999 Apr 6	IPOL	0.30 × 0.25	−34	1051	...	0.7	456	−0.5, 0.5, 1, 2, 4, 8, 16, 32, 64
		PPOL	...	...	<3.0	70	0.6	4.0	...
2200+420	1998 Jul 31	IPOL	0.31 × 0.19	−4	5303	...	1.1	3718	−0.1, 0.1, 0.2, 0.4, 0.8
		PPOL	...	...	214	123	0.8	75	...
2351+456	2000 Sep 10	IPOL	0.41 × 0.19	20	1362	...	1.1	1008	−0.35, 0.35, 0.7, 1.4, 2.8
		PPOL	...	...	24	51	0.6	18	...

NOTE.—Col. (1): Source name. Col. (2): UT Observation date. Col. (3): Image polarization type. Col. (4): FWHM dimensions of Gaussian restoring beam. Col. (5): Position angle of restoring beam. Col. (6): Total cleaned flux density. Col. (7): Electric vector scaling in image. Col. (8): Dynamic range. Col. (9): Peak intensity. Col. (10): Contour levels, expressed as a percentage of peak intensity.

[a] Image presented in Lister & Smith (2000).

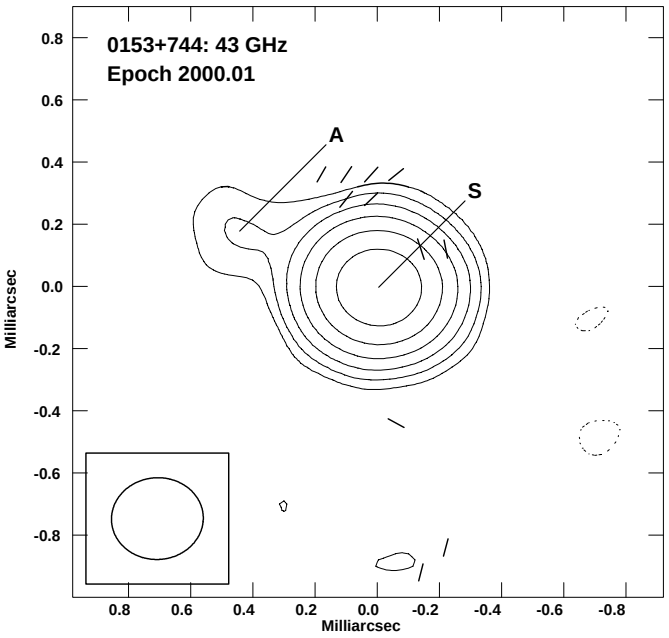

FIG. 3.—VLBA total intensity image of 0153+744 at 43 GHz, with electric vectors superimposed.

At the central position of each component, we measured the EVPA and the percentage linear polarization $m = 100P/I$, where $P = (Q^2 + U^2)^{1/2}$ and Q, U, and I are Stokes flux densities. We note that in some cases, the peak of polarized emission is offset from that of the I emission, so that the values of m given in Tables 3 and 4 may not represent the maximum percentage polarization associated with a particular component. For those components with a peak P flux density smaller than 5 times the rms noise level in the P image, we quote an upper limit on m. We make no corrections for Ricean bias in the other components, since these are all negligible.

4. DISCUSSION: CORRELATIONS AMONG SOURCE PROPERTIES

The PR sample has been extensively studied at a variety of wavelengths and resolution levels and has one of the

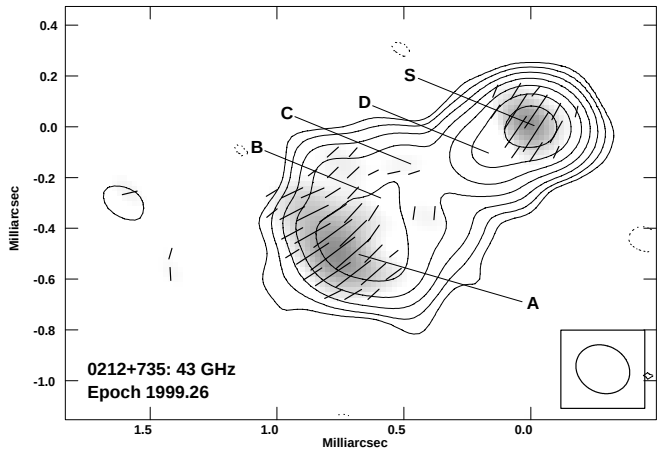

FIG. 4.—VLBA total intensity image of 0212+735 at 43 GHz, with electric vectors superimposed. The gray scale indicates linearly polarized intensity.

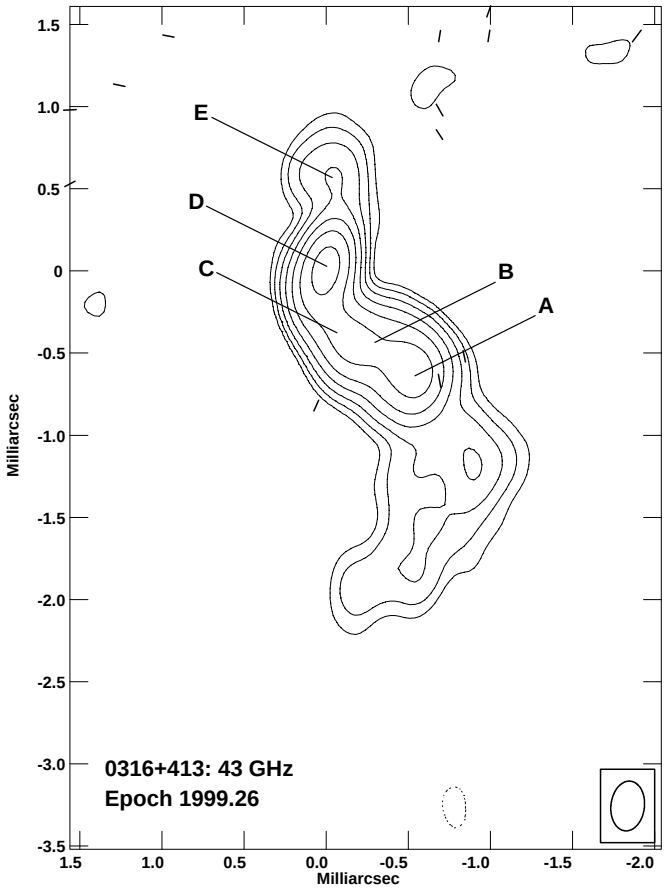

FIG. 5.—VLBA total intensity image of 0316+413 (3C 84) at 43 GHz, with electric vectors superimposed.

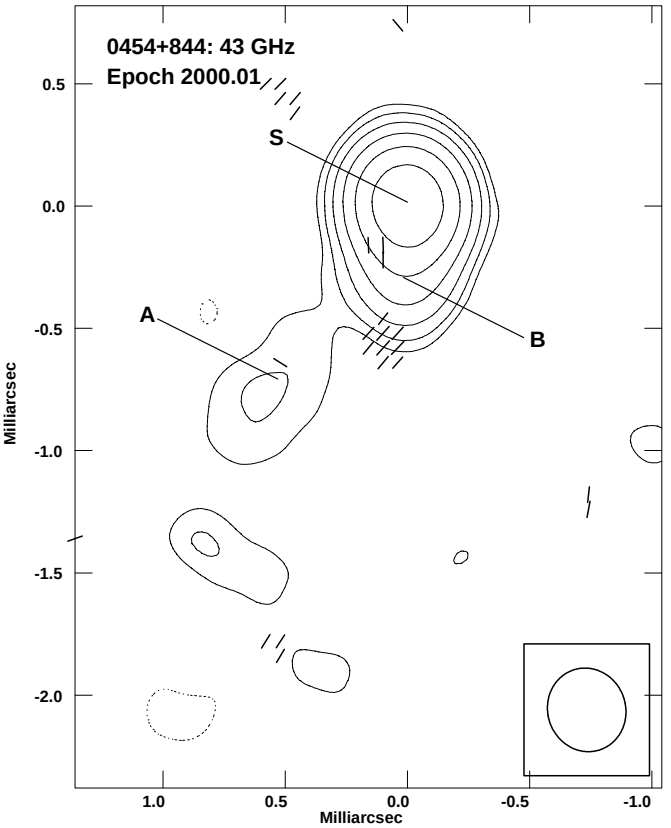

FIG. 6.—VLBA total intensity image of 0454+844 at 43 GHz, with electric vectors superimposed.

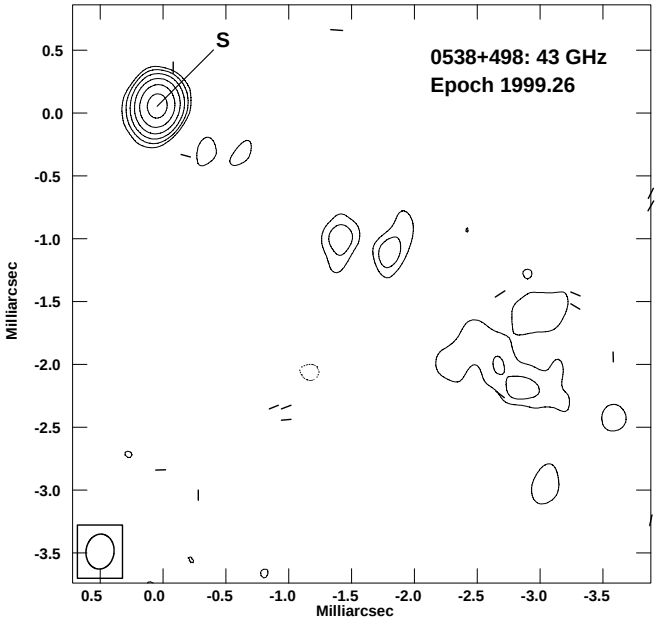

FIG. 7.—VLBA total intensity image of 0538+498 (3C 147) at 43 GHz, with electric vectors superimposed.

largest collections of published data of any radio sample. Many of these data were tabulated by Lister et al. (2001b) and are summarized here in Tables 1 and 5.

We extend the multidimensional analysis of Lister et al. (2001b) to look for trends between our measured polarization properties and various source quantities from the literature using Kendall's τ tests. For those source properties that contain measured upper or lower limits (i.e., censored data), we use a version of Kendall's τ test from the Astronomical Survival Analysis (ASURV) package (Lavalley, Isobe, & Feigelson 1992). Many of the observed properties in flux-limited AGN samples (e.g., luminosity) have a strong redshift dependence because of the lower flux cutoff and the steepness of the parent luminosity function (Padovani 1992). We therefore calculate an additional partial correlation coefficient, removing the effects of redshift (see Lister et al. 2001b) for each pair of variables. In the case of variables involving censored data, we use the algorithm of Akritas & Siebert (1996). Given the large number of tests performed, we reject any correlations with a confidence level less than $\sim$98%. We also reject any instances in which one or more outlying points artificially raise the correlation significance above this level. We give a list of significant correlations and their statistical confidence levels in Table 6.

We also perform a series of two-sample tests on the data to look for differences in properties among different source classes, such as quasars versus BL Lac objects. For the noncensored variables, we use a standard Kolmogorov-Smirnov (K-S) test, while for the censored ones, we use Gehan's generalized Wilcoxon two-sample test (Gehan 1965) from the ASURV package. We again use a 98% confidence level to determine whether any differences are significant. The results of these tests can be found in Table 7, and are discussed in § 5. Here we discuss the individual correlations we have found using Kendall's τ tests for the FS-PR sample.

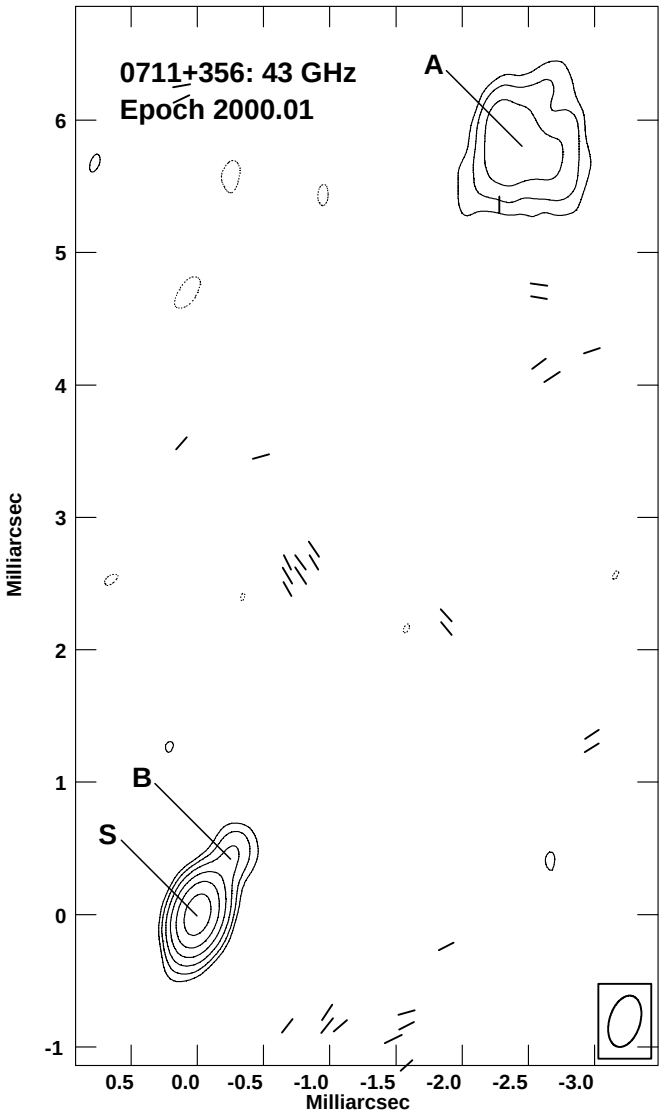

FIG. 8.—VLBA total intensity image of 0711+356 (OI 318) at 43 GHz, with electric vectors superimposed.

4.1. *Redshift*

We find that all of the luminosity-related quantities of the FS-PR sample have a strong dependence on redshift because of the flux-limited nature of the sample. This includes the variability brightness temperature (99.97% confidence; Table 6), which Lähteenmäki & Valtaoja (1999) calculated for 20 FS-PR objects by using the observed timescale of a well-defined flare at 37 GHz to estimate the size of the emitting region. The strong correlation with redshift is likely due to the fact that the variability brightness temperature is directly proportional to the observed flux density (and hence luminosity) of the flare.

4.2. *Luminosity Properties*

At 43 GHz, nearly all of the FS-PR sources have radio morphologies that are dominated by a strong core component located near the base of an extended jet. Multifrequency studies have shown that these cores have flat or inverted spectra and likely represent the region where the jet becomes optically thick. The core in lower frequency VLBI images often turns out to be a blend of two or more

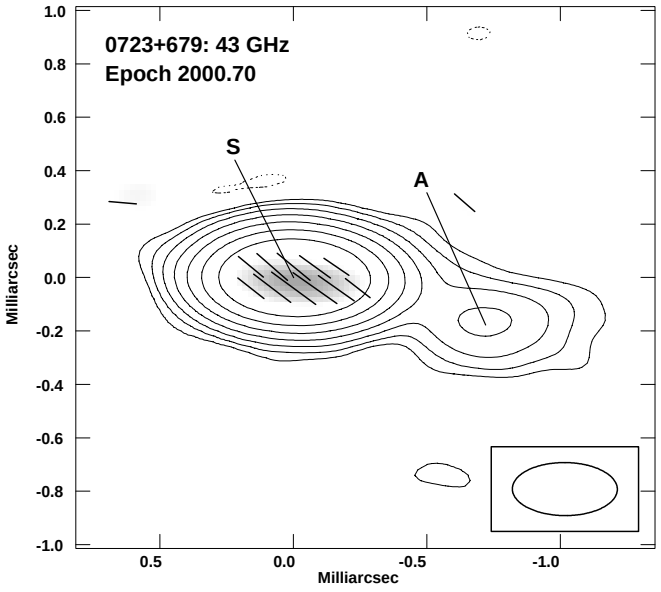

FIG. 9.—VLBA total intensity image of 0723+679 (3C 179) at 43 GHz, with electric vectors superimposed. The gray scale indicates linearly polarized intensity.

components because of insufficient spatial resolution (Lister & Smith 2000). For the majority of the FS-PR sources, our 43 GHz observations represent the highest resolution images obtained to date and are less subject to possible blending effects.

We have searched for trends between the luminosity of the VLBI core at 43 GHz and luminosities at other wavelengths using the partial correlation coefficients described in § 4. We find that both the total VLBI luminosity of the source and the luminosity of the VLBI core are well correlated with (1) the VLBI core luminosity at 5 GHz and (2) the X-ray luminosity at 1 keV (L_X). Bloom et al. (1999) found a

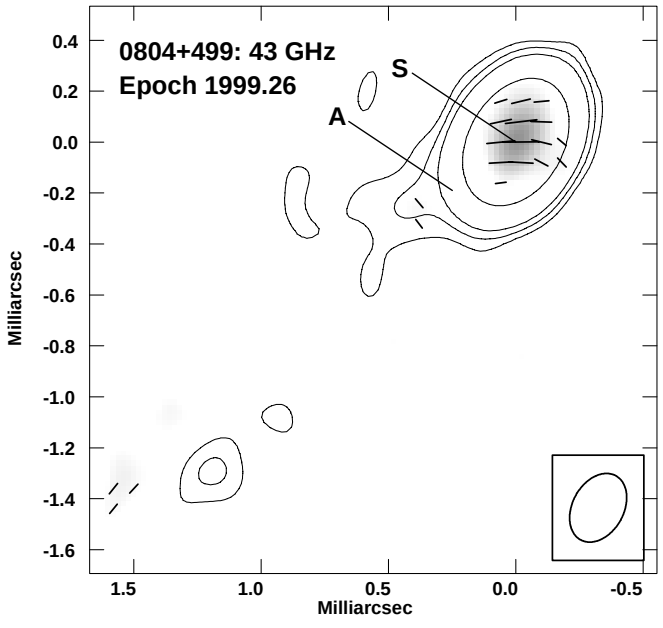

FIG. 10.—VLBA total intensity image of 0804+499 (OJ 508) at 43 GHz, with electric vectors superimposed. The gray scale indicates linearly polarized intensity.

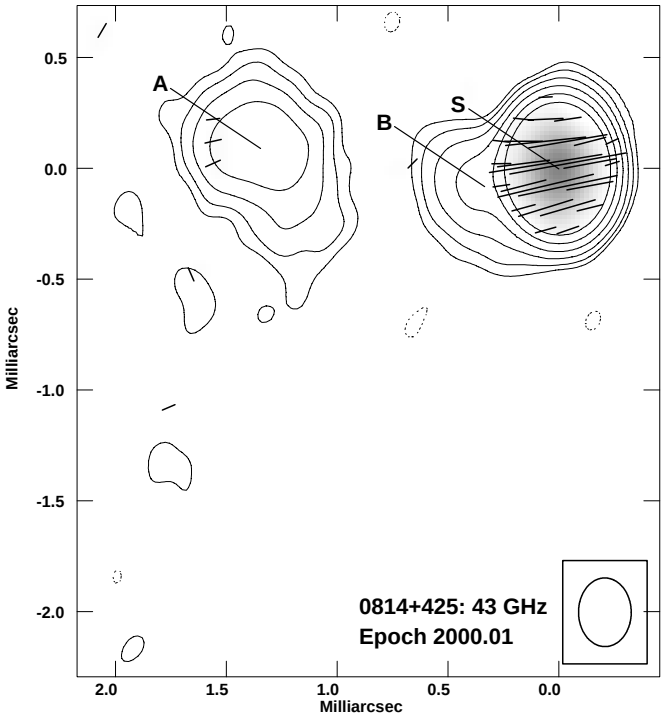

FIG. 11.—VLBA total intensity image of 0814+425 (OJ 425) at 43 GHz, with electric vectors superimposed. The gray scale indicates linearly polarized intensity.

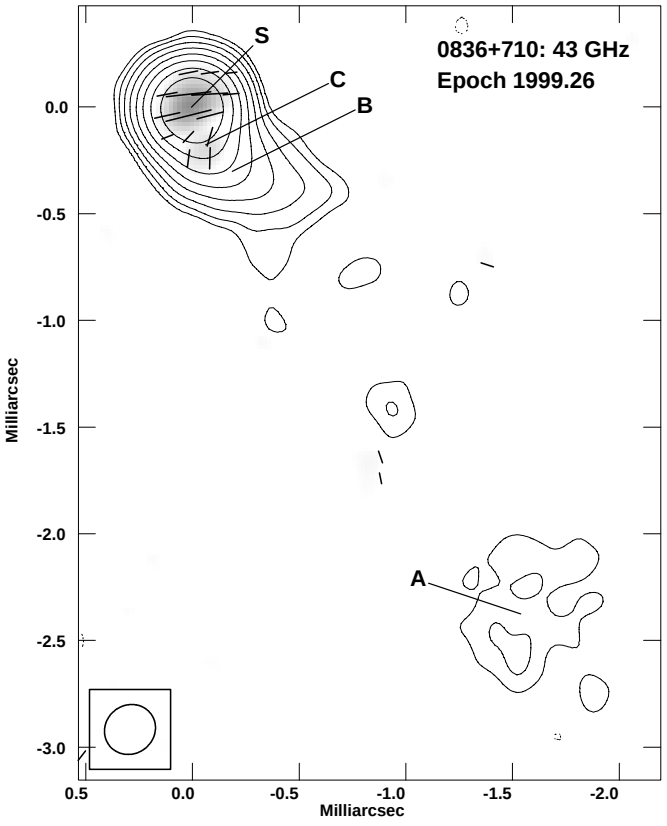

FIG. 12.—VLBA total intensity image of 0836+710 (4C 71.07) at 43 GHz, with electric vectors superimposed. The gray scale indicates linearly polarized intensity.

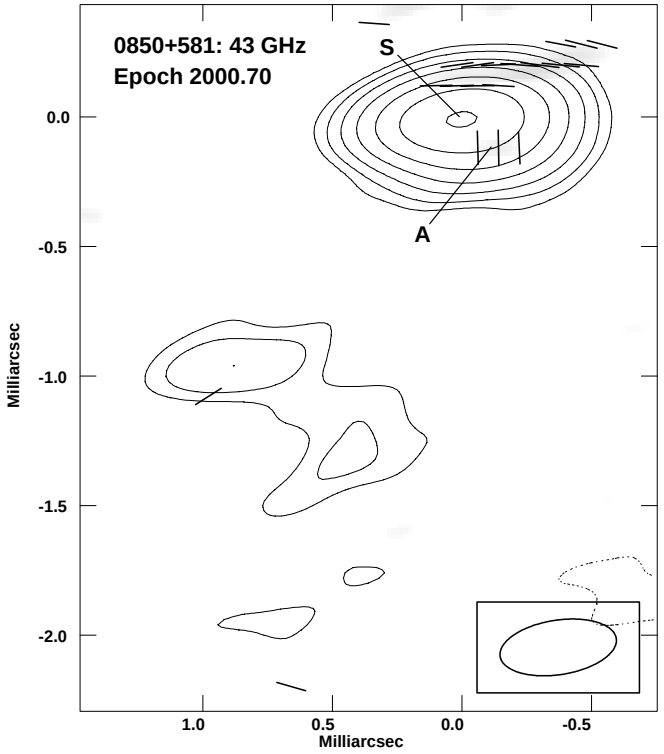

FIG. 13.—VLBA total intensity image of 0850+581 (4C 58.17) at 43 GHz, with electric vectors superimposed. The gray scale indicates linearly polarized intensity.

correlation between 22 GHz VLBI core luminosity and L_X using a different flat-spectrum AGN sample and attributed it to a common synchrotron origin for these spectral components. We also detect a correlation between 43 GHz VLBI core luminosity and optical luminosity (see Table 6). Taken together, these findings suggest that there is a well-defined synchrotron component in these AGNs whose emission extends from millimeter wavelengths through optical to X-ray energies.

4.3. *Core Dominance*

The highly core-dominated nature of the FS-PR sample is a reflection of its selection criteria and the dimming of steep-spectrum jet emission at high frequency. In order to investigate possible correlations between core dominance and other properties, we define a parameter R (col. [7] of Table 3) as the flux density of the core divided by the remaining (jet) flux density in the VLBI image. We correct the core dominance to the quasar rest frame by assuming typical spectral indices of 0 and -0.8 for the core and jet emission, respectively. The R-values range from 0.02 to ~ 20, with a median of 0.75. This suggests that most bright, flat-spectrum AGNs should be excellent targets for next-generation high-frequency space-VLBI missions, since they are likely compact enough to have sufficient flux density for fringe detection on extremely long baselines.

Our R-parameter is somewhat analogous to the core-dominance parameter F_c of Pearson & Readhead (1988), which they defined as the ratio of VLBI core-to-total (single-dish) flux density of the source at 5 GHz. The F_c-parameter is considered to be a good indicator of Doppler beaming, which causes a dramatic boosting of the jet and core fluxes in relativistic jets viewed nearly end-on. The

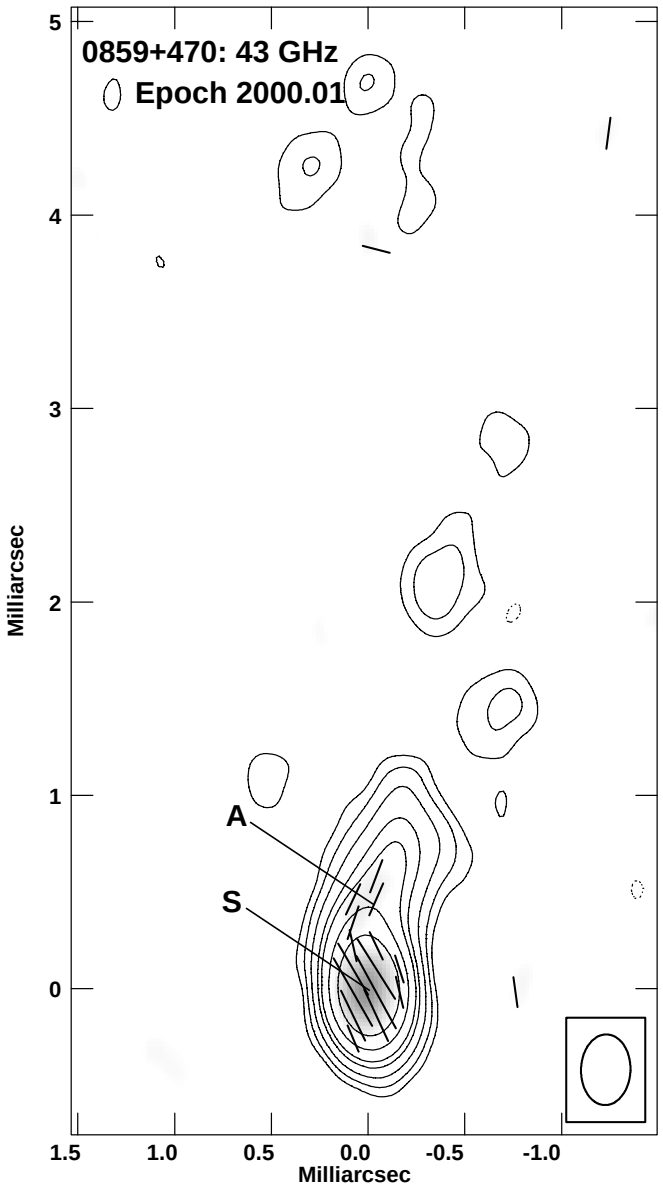

FIG. 14.—VLBA total intensity image of 0859+470 (4C 47.29) at 43 GHz, with electric vectors superimposed. The gray scale indicates linearly polarized intensity.

extended radio lobes of AGNs are not as affected by beaming, since their bulk motions are nonrelativistic. Therefore, the ratio of core-to-total flux density will increase as an AGN is viewed closer to the jet axis. This effect appears to be responsible for the well-known correlations between core dominance and (1) optical polarization (Impey, Lawrence, & Tapia 1991) and (2) 5 GHz radio variability (Aller et al. 1992) seen in the full PR sample. The latter two quantities are correlated with our R-parameter at the 99.89% and 99.45% confidence level, respectively. We find a good correlation (98.93% confidence; Fig. 33) between R and another quantity known to be influenced by beaming, namely, the variability brightness temperature (Lähteenmäki & Valtaoja 1999).

The number of correlations between our R-parameter and other known beaming indicators is somewhat surprising, since there is strong evidence (e.g., from rapid flux variability and superluminal motions) that *both* the core and jet emission on VLBI scales are beamed. Nevertheless,

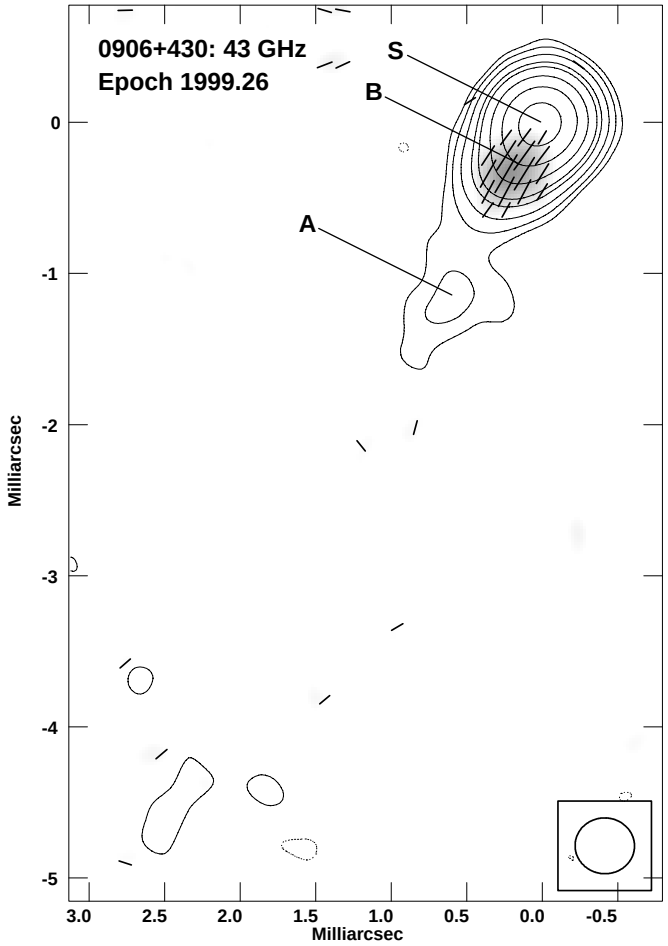

FIG. 15.—VLBA total intensity image of 0906+430 (3C 216) at 43 GHz, with electric vectors superimposed. The gray scale indicates linearly polarized intensity.

we find evidence that the ratio of core-to-jet flux is higher in the more highly beamed sources. This runs contrary to the predictions of the standard jet model, which suggests that the core emission should be *less* boosted than that of the jet. Since the jet emission is dominated by components with finite lifetimes, its emission is boosted by a factor of $\delta^{3-\alpha}$,

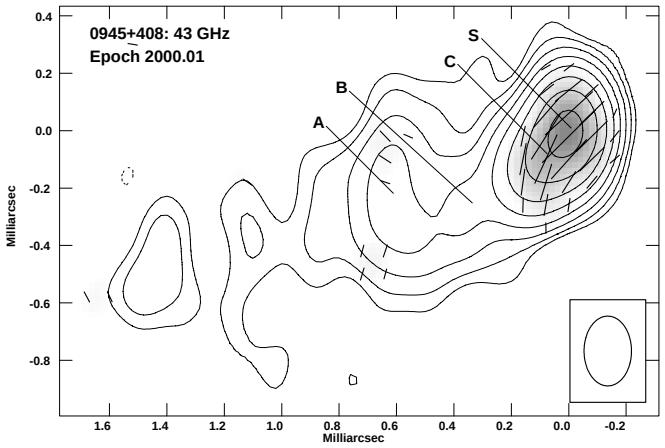

FIG. 16.—VLBA total intensity image of 0945+408 (4C 40.24) (3C 179) at 43 GHz, with electric vectors superimposed. The gray scale indicates linearly polarized intensity.

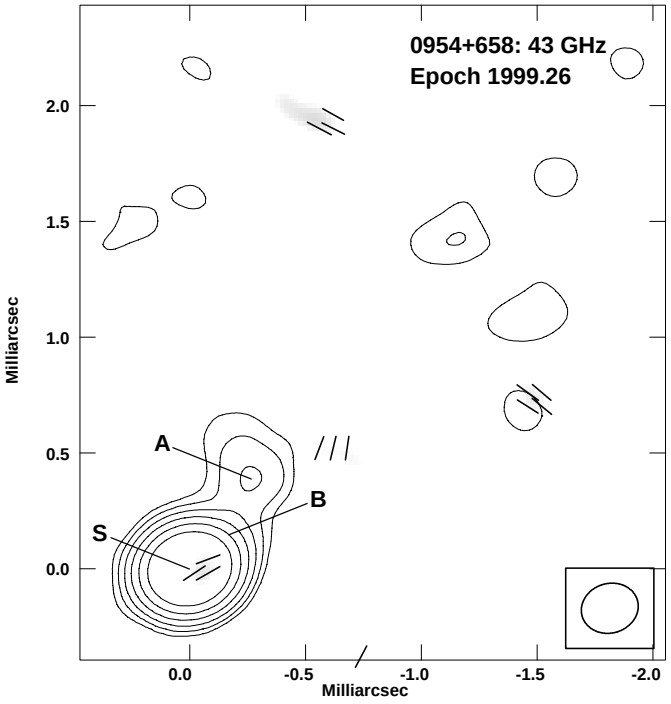

FIG. 17.—VLBA total intensity image of 0954+658 at 43 GHz, with electric vectors superimposed. The gray scale indicates linearly polarized intensity.

where δ is the Doppler factor of the bulk flow. The core, on the other hand, is only boosted by a factor of $\delta^{2-\alpha}$.

These apparent contradictions can be resolved by considering several other effects that can influence the R-values of beamed sources. First, we expect the high-energy electrons that are accelerated in the cores to experience inverse-Compton losses from scattering off of external photons. These losses are larger for highly beamed sources because of blueshifting of the external photons in the rest frame of the jet (e.g., Dermer & Schlickeiser 1993). According to the shock-in-jet model of Marscher & Gear (1985), the lifetimes of components that evolve adiabatically as they move down the jet are shortened accordingly because of the steepening of their electron energy distribution and the shifting of the high-energy electron cutoff into the radio region. This tends to reduce the jet flux relative to the core and increase R. Second, highly beamed sources tend to have faster com-

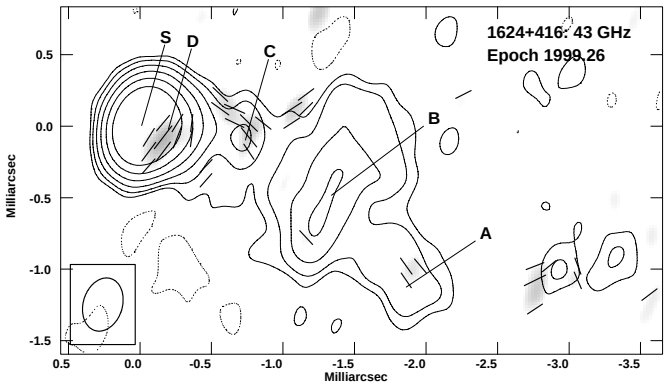

FIG. 18.—VLBA total intensity image of 1624+416 (4C 41.32) at 43 GHz, with electric vectors superimposed. The gray scale indicates linearly polarized intensity.

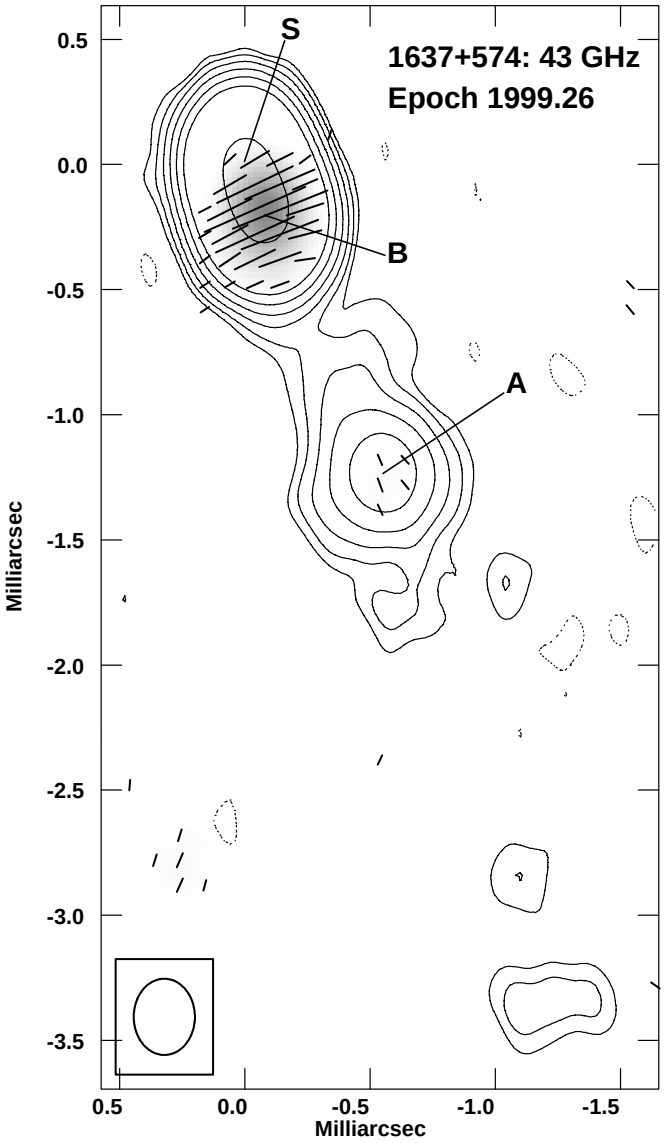

FIG. 19.—VLBA total intensity image of 1637+574 (OS 562) at 43 GHz, with electric vectors superimposed. The gray scale indicates linearly polarized intensity.

ponent motions, which causes the jet components to fade out more rapidly, thereby reducing the total jet flux and lowering the number of components per unit length in the jet. Third, it is possible that the bulk speed of the flow is higher in the cores than farther down the jet, which would

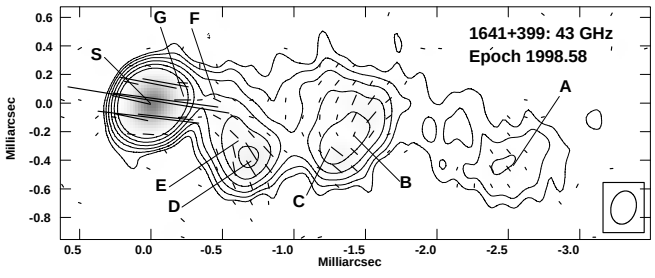

FIG. 20.—VLBA total intensity image of 1641+399 (3C 345) at 43 GHz, with electric vectors superimposed. The gray scale indicates linearly polarized intensity.

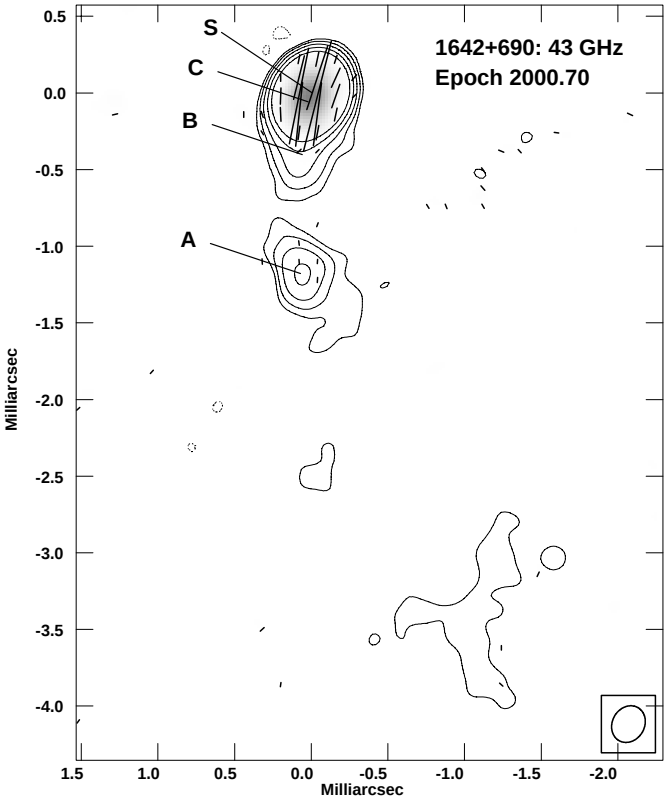

FIG. 21.—VLBA total intensity image of 1642+690 (4C 69.21) at 43 GHz, with electric vectors superimposed. The gray scale indicates linearly polarized intensity.

lead to a higher amount of beaming in the core. Finally, the standard jet model predictions are based on the assumption that the core emission originates from a continuous jet; however, our VLBI "cores" may include emission from unresolved components very close to the base of the jet, which have finite lifetimes.

4.4. *Fractional Polarization of Core Components*

The fractional polarizations of the VLBI core components in our sample range up to 9%, with most being weakly polarized ($\lesssim$2%). The integrated VLBI fractional polarization [defined as the ratio of $(Q^2 + U^2)^{1/2}$ to I, where Q, U, and I represent the cleaned Stokes fluxes in the VLBI images] has a similar distribution to that of the cores (Fig. 34). This is simply a reflection of the dominance of the core

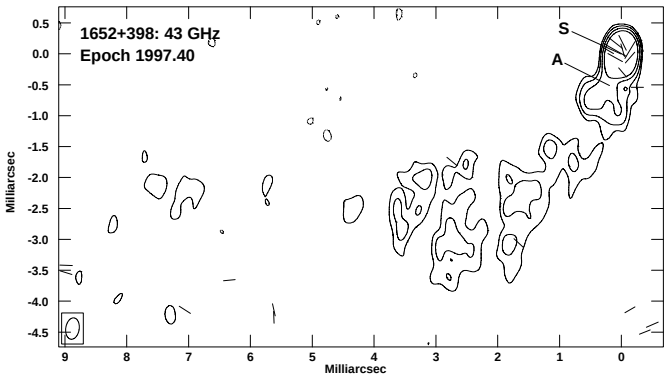

FIG. 22.—VLBA total intensity image of 1652+398 (MK 501) at 43 GHz, with electric vectors superimposed.

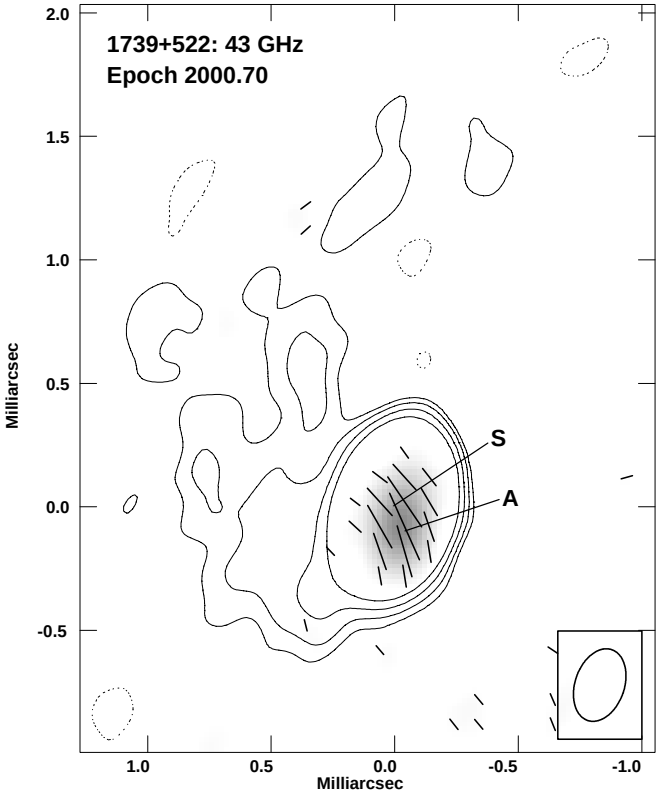

FIG. 23.—VLBA total intensity image of 1739+522 (4C 51.37) at 43 GHz, with electric vectors superimposed. The gray scale indicates linearly polarized intensity.

component and the relatively weak contribution of the steep-spectrum jet to the polarized flux at 43 GHz. Indeed, we find that the core and integrated VLBI polarization levels are correlated at the 99.995% confidence level.

We find that sources with flatter spectra between 5 and 15 GHz tend to have higher core and integrated VLBI fractional polarizations at 43 GHz (Fig. 35). The simplest means of obtaining a flatter overall radio spectrum is to increase the dominance of the core component, since its spectrum is usually flatter than the jet. The correlations in Figure 35 may therefore be due to a separate correlation between polarization and core dominance. There is some indication that the 43 GHz core fractional polarization may be corre-

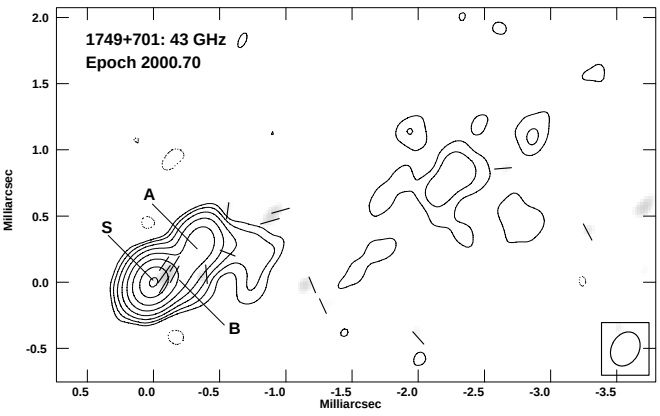

FIG. 24.—VLBA total intensity image of 1749+701 at 43 GHz, with electric vectors superimposed. The gray scale indicates linearly polarized intensity.

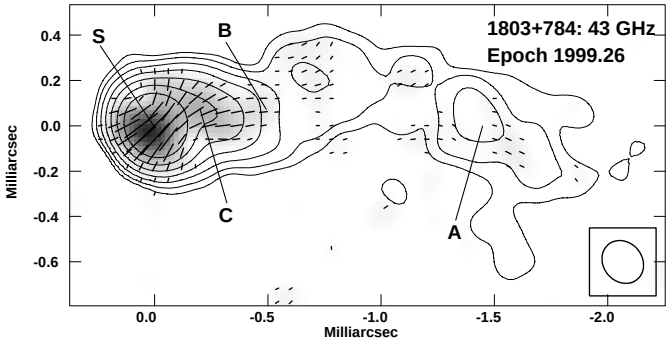

FIG. 25.—VLBA total intensity image of 1803+784 at 43 GHz, with electric vectors superimposed. The gray scale indicates linearly polarized intensity.

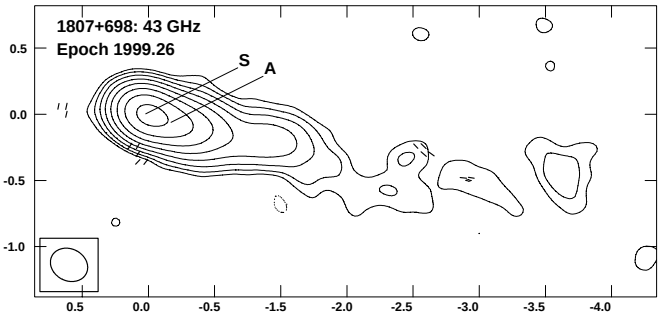

FIG. 26.—VLBA total intensity image of 1807+698 (3C 371) at 43 GHz, with electric vectors superimposed.

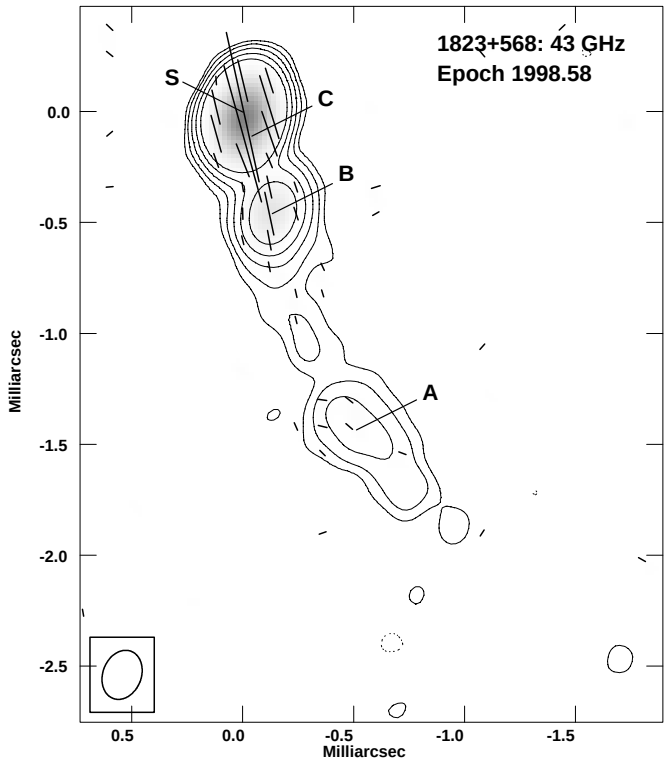

FIG. 27.—VLBA total intensity image of 1823+568 (4C 56.27) at 43 GHz, with electric vectors superimposed. The gray scale indicates linearly polarized intensity.

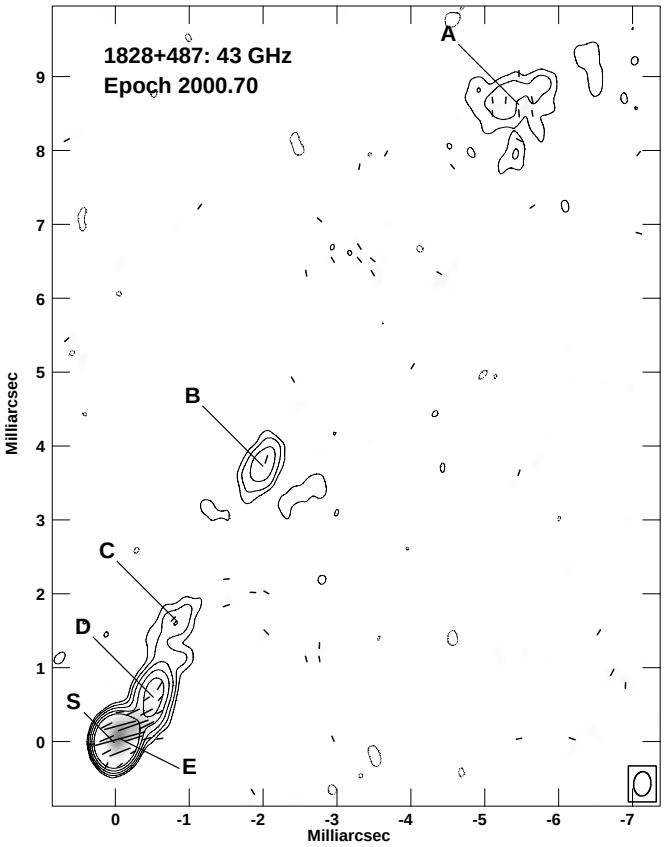

FIG. 28.—VLBA total intensity image of 1828+487 (3C 380) at 43 GHz, with electric vectors superimposed. The gray scale indicates linearly polarized intensity.

lated with the 5 GHz core dominance (F_c) in our sample, but only at the 94.5% confidence level, which is below our significance cutoff. It is not clear whether such a trend, if it exists, could either be the result of relativistic beaming effects or an intrinsic property of the cores.

We find that the fractional polarization of the core component at 43 GHz is also related to the overall optical polarization of the source. Lister & Smith (2000) found such a trend in a sample of lowly and highly optically polarized quasars, which suggested a common (possibly cospatial)

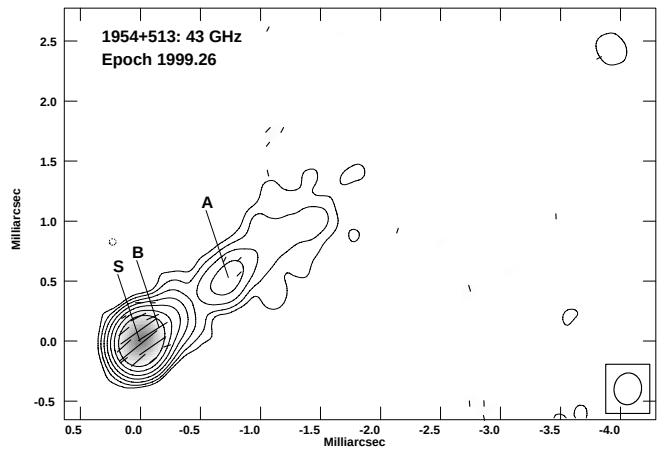

FIG. 29.—VLBA total intensity image of 1954+513 (OV 591) at 43 GHz, with electric vectors superimposed. The gray scale indicates linearly polarized intensity.

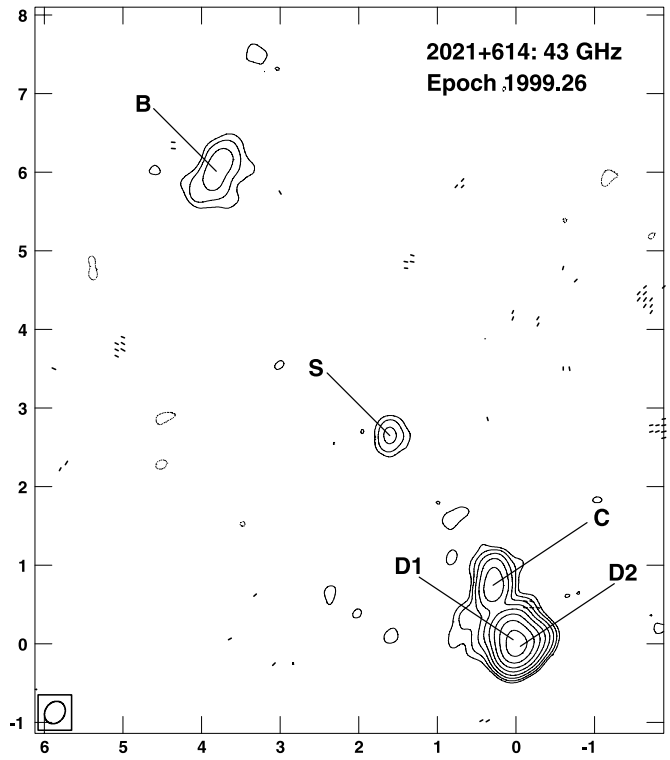

FIG. 30.—VLBA total intensity image of 2021+614 (OW 637) at 43 GHz, with electric vectors superimposed.

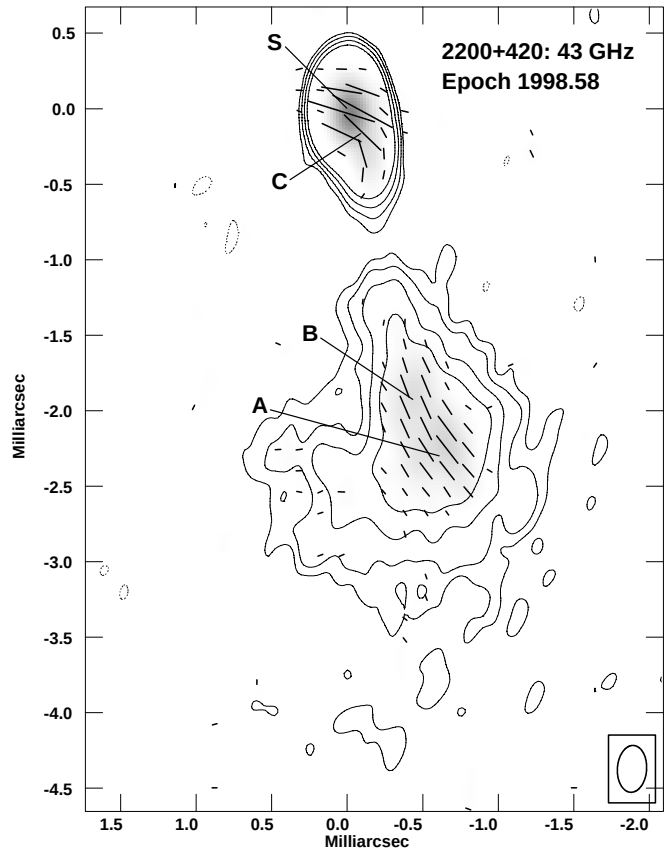

FIG. 31.—VLBA total intensity image of 2200+420 (BL Lac) at 43 GHz, with electric vectors superimposed. The gray scale indicates linearly polarized intensity.

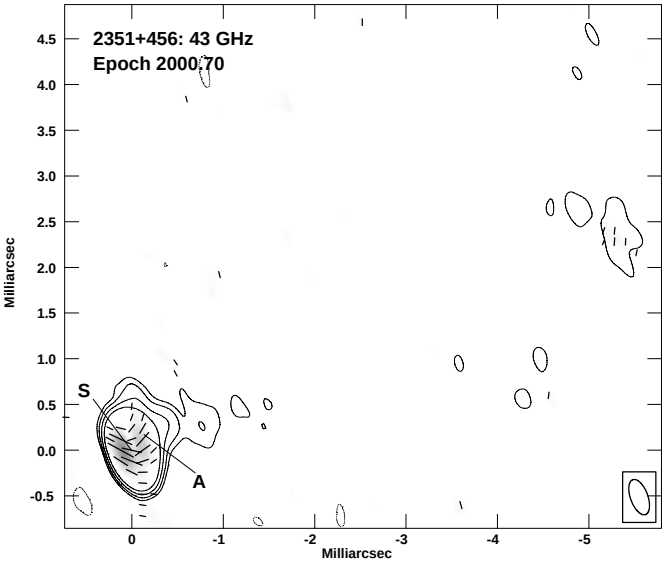

FIG. 32.—VLBA total intensity image of 2351+456 (4C 45.51) at 43 GHz, with electric vectors superimposed. The gray scale indicates linearly polarized intensity.

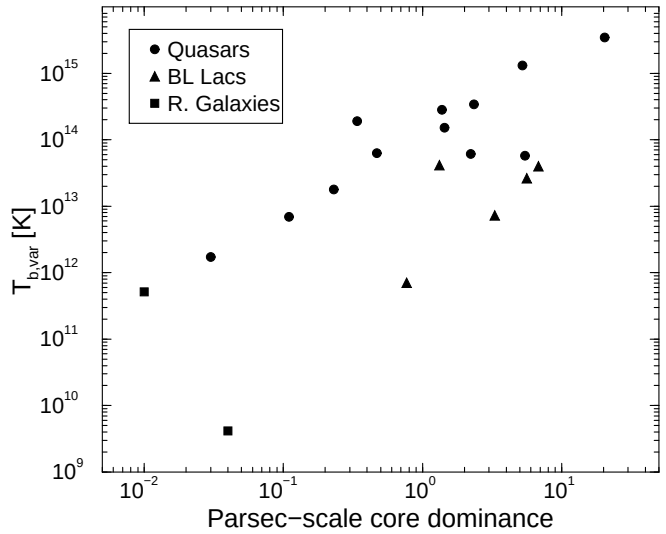

FIG. 33.—Variability brightness temperature at 37 GHz vs. parsec-scale core dominance (R) at 43 GHz.

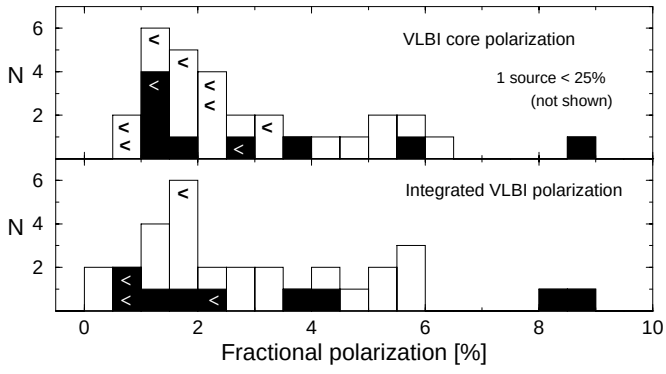

FIG. 34.—*Top*: Fractional polarization distribution of FS-PR core components at 43 GHz. *Bottom*: Integrated 43 GHz VLBI fractional polarization distribution of FS-PR sources. The shaded boxes in both panels represent BL Lac objects.

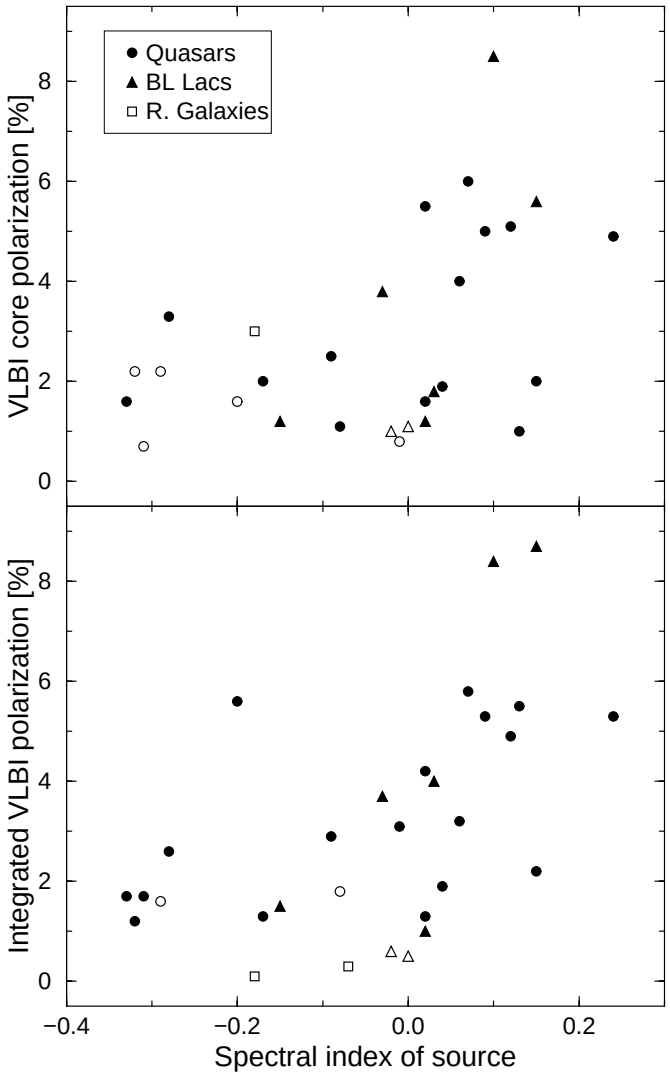

FIG. 35.—*Top*: Fractional polarization of VLBI core components at 43 GHz plotted against mean 5–15 GHz spectral index of the source. *Bottom*: Integrated 43 GHz VLBI fractional polarization plotted against mean 5–15 GHz spectral index of the source. The unshaded symbols denote upper limits in fractional polarization.

origin for the emission at these frequencies. In Figure 36, we plot these two quantities for the FS-PR sample. The optical polarization data are tabulated in Table 1 and are taken from Impey et al. (1991), with the exception of the data from 1954+513, which are taken from Wills et al. (1992). These authors attempted to reduce possible biases by taking the first reliable published optical polarization measurement for each source. We note that the optical polarization levels of flat-spectrum radio-loud AGNs are highly variable, which introduces a large degree of scatter in the y-axis of Figure 36 because of the nonsimultaneity of the radio and optical measurements. Nevertheless, there appears to be a positive trend present among objects with $m_{\rm opt} \gtrsim 1\%$. There is no trend among the low-polarization objects, however. In order for them to follow the main trend, their current optical polarization levels would have to be significantly higher than those measured by Impey et al. (1991). This appears to be the case for at least one FS-PR source: 1633+382, whose optical polarization had never exceeded 3% until recent observations showed variable $m_{\rm opt}$ levels

TABLE 3

PROPERTIES OF PEARSON-READHEAD VLBI CORES AT 43 GHZ

Source (1)	S (mJy) (2)	log L_{core} (W Hz^{-1}) (3)	m_{core} (%) (4)	EVPA (deg) (5)	|EVPA − JPA| (deg) (6)	R (7)	Major Axis (mas) (8)	a (9)	P.A. (deg) (10)
FS-PR Sample Objects									
0016+731.....	616	27.71	2.0	89	43	5.23	0.06	0.44	83
0133+476.....	4016	27.87	4.9	−36	6	5.46	0.07	0.67	2
0212+735.....	467	27.84	5.1	−33	26	0.23	0.09	0.18	94
0316+413.....	169	23.10	<3.0	...	...	0.04	0.26	0.57	77
0454+844.....	77	24.39	<2.5	...	...	2.44	0.00	...	...
0723+679.....	677	27.08	2.0	52	24	11.86	0.10	0.43	72
0804+499.....	704	27.57	1.6	−88	35	20.34	0.03	0.24	135
0814+425.....	750	26.05	3.8	−80	4	5.62	0.07	0.44	43
0836+710.....	1114	28.14	1.6	−80	79	1.38	0.07	0.27	56
0850+581.....	190	26.93	<2.2	...	...	1.10	0.00	...	...
0859+470.....	262	27.16	3.3	30	33	1.00	0.00	...	...
0906+430.....	363	26.61	<0.7	...	...	1.78	0.13	0.37	146
0923+392.....	298	26.56	<1.6	...	...	0.03	0.06	0.23	108
0945+408.....	465	27.27	5.5	−46	3	0.34	0.00	...	...
0954+658.....	402	26.13	1.2	−58	9	6.81	0.02	0.74	108
1624+416.....	206	27.55	<2.2	...	...	0.56	0.00	...	...
1633+382.....	1754	28.17	2.5	24	75	1.44	0.09	0.31	1
1637+574.....	800	27.05	1.0	−54	74	0.47	0.04	0.23	21
1641+399.....	6234	27.74	5.0	81	23	2.22	0.14	0.16	89
1642+690.....	892	27.10	6.0	−14	8	1.68	0.00	...	...
1652+398.....	278	23.88	1.2	27	47	1.48	0.13	0.86	95
1739+522.....	645	27.50	1.9	34	10	2.35	0.08	0.55	177
1749+701.....	199	26.47	<1.0	...	...	0.81	0.05	0.56	119
1803+784.....	1242	27.16	5.6	−45	24	1.32	0.06	0.82	162
1807+698.....	326	24.32	<1.1	...	...	0.77	0.07	0.29	78
1823+568.....	1065	27.07	8.5	13	8	2.04	0.06	0.44	169
1928+738.....	298	25.83	<0.8	...	...	0.11	0.03	0.73	69
1954+513.....	774	27.47	4.0	−52	1	1.77	0.07	0.34	138
2021+614.....	12	24.20	<25.0	...	...	0.01	0.00	...	...
2200+420.....	4123	25.69	1.8	73	44	3.31	0.07	0.22	40
2351+456.....	1209	28.10	1.1	77	64	3.29	0.13	0.46	95
Other PR Sample Objects									
0153+744.....	84	27.08	<2.5	...	...	10.68	0.07	0.16	35
0538+498.....	177	26.12	<3.2	...	...	1.15	0.05	0.51	99
0711+356.....	73	26.69	<2.8	...	...	0.69	0.00	...	...
1828+487.....	649	26.89	2.1	−72	23	0.73	0.09	0.19	68

NOTE.—All derived quantities are calculated assuming $h = 0.65$, $q_0 = 0.1$, and a zero cosmological constant. Col. (1): IAU source name. Col. (2): Flux density of core component. Col. (3): Luminosity of core component. Col. (4): Fractional polarization of core component. Col. (5): EVPA of core component. Col. (6): Offset of EVPA of core with respect to the innermost jet direction. Col. (7): Ratio of VLBI core-to-remaining VLBI flux density (source frame). Col. (8): FWHM major axis of fitted Gaussian component. A value of zero denotes a δ-function component. Col. (9): Axial ratio of fitted component. Col. (10): Position angle of component's major axis.

between $\sim$1.5% and 7% (P. S. Smith 2001, private communication).

There has been a historical trend among optical astronomers to divide quasars into low and high optical polarization classes at $m_{opt} \simeq 3\%$, since most optically selected quasars rarely exceed this value (Berriman et al. 1990). This division is somewhat more problematic for flat-spectrum radio-loud AGNs, since their optical polarizations are known to be highly variable. Following the standard convention, we classify any source having a single measurement of $m_{opt} > 3\%$ as a "high optical polarization quasar" (HPQ). In order to alleviate possible bias, we have only classified sources as "low-polarization radio quasars" (LPRQs) in Table 1 if they have had at least three published optical polarization measurements and have never had $m_{opt} > 3\%$. Unfortunately, this leaves only five genuine LPRQs in the FS-PR sample, which is too small a sample for statistical comparisons. This underscores the need for more frequent optical polarization monitoring of larger samples of core-dominated AGNs for better understanding the connection between the radio and optical regimes.

4.5. *Electric Vector Orientation of Core Components*

The EVPA of a polarized jet component with respect to the local jet direction (|EVPA − JPA|) is an important quantity for testing the predictions of shock models for AGNs (e.g., Laing 1980; Hughes et al. 1985). These models suggest that transverse planar shocks form in the flow and preferentially compress the perpendicular component of the magnetic field. At high frequencies, at which the emission is optically thin, this generally renders the observed electric vector parallel to the jet axis and raises the fractional polar-

TABLE 4

JET COMPONENT PROPERTIES

Source (1)	Name (2)	d (mas) (3)	P.A. (deg) (4)	S (mJy) (5)	log L (W Hz $^{-1}$) (6)	m (%) (7)	EVPA (deg) (8)	JPA_{in} (deg) (9)	JPA_{out} (deg) (10)	Major Axis (mas) (11)	a (12)	P.A. (deg) (13)
FS-PR Sample Objects												
0016+731.....	A	0.93	132	50	26.97	<36	...	132	105	0.74	0.45	115
0133+476.....	B	0.09	330	384	27.07	5.4	143	330	331	0.27	0.37	174
	A	0.53	331	41	26.10	<19	...	331	331	0.30	0.50	52
0212+735.....	D	0.21	121	231	27.96	<2.8	...	121	98	0.16	0.64	115
	C	0.51	107	36	27.15	11.0	111	98	138	0.00	...	...
	B	0.67	115	223	27.94	<7.3	...	138	159	0.44	0.43	65
	A	0.86	126	267	28.02	17.4	133	159	...	0.35	0.45	70
0316+413.....	D	0.55	176	1165	23.94	<0.6	...	176	188	0.20	0.32	155
	C	0.95	182	783	23.77	<1.3	...	188	257	0.56	0.10	38
	B	1.04	195	765	23.76	<1.4	...	257	231	0.45	0.36	63
	A	1.31	203	734	23.74	<1.0	...	231	212	0.23	0.87	5
0454+844.....	B	0.31	177	14	23.68	<13	...	177	308	0.00	...	...
	A	0.90	144	7	23.38	...	...	308	...	0.65	0.12	145
0723+679.....	A	0.75	256	30	25.94	<19	...	256	...	0.06	1.00	173
0804+499.....	A	0.32	127	20	26.33	<17	...	127	...	0.92	0.16	103
0814+425.....	B	0.35	103	34	24.79	12.9	84	103	103	0.29	0.61	96
	A	1.35	86	67	25.08	<12	...	81	167	0.40	0.67	65
0836+710.....	C	0.19	201	175	27.74	2.2	171	201	225	0.11	0.14	50
	B	0.36	212	75	27.37	<3.8	...	225	213	0.26	0.48	77
	A	2.84	213	35	27.04	...	...	213	...	0.58	0.83	31
0850+581.....	A	0.17	227	53	26.67	< 5.6	...	227	153	0.00	...	...
0859+470.....	A	0.45	357	92	27.02	7.4	157	357	336	0.66	0.15	156
0906+430.....	B	0.32	151	95	26.21	7.5	146	151	152	0.26	0.51	139
	A	1.29	153	19	25.51	<36	...	152	152	0.97	0.17	153
0923+392.....	e	1.05	93	36	25.83	<40	...	93	123	0.28	0.50	150
	d	1.38	101	48	25.95	<21	...	123	135	0.26	0.16	164
	C	1.79	109	102	26.28	<15	...	135	77	0.33	0.45	152
	b	2.17	103	69	26.11	<9.7	...	77	94	0.00	...	...
	A	2.83	101	2027	27.58	5.7	71	94	81	0.00	...	...
0945+408.....	C	0.13	137	455	27.54	5.9	154	137	122	0.20	0.18	134
	B	0.44	127	113	26.94	<14	...	122	262	0.35	0.36	142
	A	0.66	110	85	26.81	<12	...	262	108	0.34	0.49	176
0954+658.....	B	0.23	311	8	24.54	<8.3	...	311	337	0.00	...	...
	A	0.48	326	13	24.75	<37	...	337	0	0.00	...	...
1624+416.....	D	0.19	262	62	27.47	6.1	144	262	262	0.18	0.48	99
	C	0.74	262	10	26.68	...	...	262	237	0.00	...	...
	B	1.42	250	49	27.37	<38	...	237	219	0.85	0.21	160
	A	2.17	239	7	26.52	...	...	219	0.00	0.00	...	...
1633+382.....	c2	0.10	279	92	27.25	2.0	21	279	264	0.28	0.43	99
	c1	0.47	267	41	26.90	8.7	116	264	317	0.09	0.47	153
	B	0.81	291	50	26.99	<16	...	360	268	0.36	0.28	167
	A	2.02	269	49	26.98	<18	...	268	288	0.32	0.67	126
1637+574.....	B	0.23	200	988	27.34	3.8	113	200	205	0.09	0.58	44
	A	1.37	204	71	26.20	9.9	24	205	200	0.20	0.83	64
1641+399.....	G	0.24	284	144	26.27	5.0	89	284	262	0.00	...	...
	F	0.45	274	30	25.59	14.7	63	262	210	0.00	...	...
	E	0.66	247	547	26.85	8.1	39	210	210	0.34	0.67	32
	D	0.81	240	175	26.35	11.3	32	210	294	0.00	...	...
	C	1.29	256	122	26.20	7.0	53	263	298	0.00	...	...
	B	1.44	261	395	26.71	2.7	150	300	300	0.33	0.62	145
	A	2.56	260	146	26.27	27.9	37	247	247	0.46	0.64	114
1642+690.....	C	0.07	158	257	26.76	6.7	169	158	171	0.14	0.70	176
	B	0.42	171	31	25.84	19.8	132	171	180	0.28	0.68	5
	A	1.19	177	28	25.79	12.5	173	180	205	0.24	0.18	24
1652+398.....	A	0.55	160	67	23.28	<33	...	160	160	0.95	0.55	163
1739+522.....	A	0.12	204	79	26.89	3.5	22	204	126	0.00	...	...
1749+701.....	B	0.21	275	16	25.58	<5.1	...	275	329	0.00	...	...
	A	0.42	307	82	26.29	<5.1	...	329	277	0.29	0.39	158
1803+784.....	C	0.22	291	307	26.73	16.0	123	291	270	0.27	0.46	72
	B	0.51	279	169	26.47	39.0	94	270	284	0.72	0.33	120
	A	1.46	270	140	26.39	<18	...	236	236	0.63	0.47	58
1807+698.....	A	0.21	252	190	24.10	<1.5	...	252	257	0.14	0.61	83

TABLE 4—*Continued*

Source (1)	Name (2)	d (mas) (3)	P.A. (deg) (4)	S (mJy) (5)	log L (W Hz $^{-1}$) (6)	m (%) (7)	EVPA (deg) (8)	JPA_{in} (deg) (9)	JPA_{out} (deg) (10)	Major Axis (mas) (11)	a (12)	P.A. (deg) (13)
1823+568.....	C	0.12	201	109	26.26	13.3	21	201	195	0.00	...	...
	B	0.48	196	148	26.39	21.6	11	195	201	0.13	0.56	173
	A	1.52	200	48	25.90	41.7	41	201	226	0.32	0.44	56
1928+738.....	G	0.24	166	1338	26.58	2.7	100	166	159	0.09	0.44	3
	f2	0.54	162	209	25.77	<2.0	...	159	168	0.14	0.73	150
	f1	0.76	164	14	24.60	<8.5	...	168	127	0.00	...	...
	e2	1.06	153	87	25.39	7.0	82	127	159	0.18	0.55	147
	e1	1.42	155	260	25.87	<3.4	...	159	205	0.38	0.59	167
	D	1.66	164	18	24.71	<14	...	205	149	0.00	...	...
	C	2.77	158	38	25.03	<18	...	149	254	0.35	0.41	55
	B	2.74	168	8	24.35	28	71	254	171	0.00	...	...
	A	3.20	168	11	24.49	19	41	171	311	0.00	...	...
1954+513.....	B	0.20	307	135	26.99	3.6	120	307	307	0.29	0.33	129
	A	0.91	306	59	26.63	<14	...	307	307	0.36	0.38	135
2021+614.....	B	4.04	33	45	24.84	<20	...	33	...	0.57	0.49	148
	C	2.30	214	115	25.25	<5	...	214	201	0.42	0.08	177
	D1	3.03	211	594	25.96	<0.7	...	201	222	0.35	0.38	15
	D2	3.15	212	262	25.61	<0.7	...	222	...	0.29	0.16	125
2200+420.....	C	0.19	209	686	24.94	3.3	46	209	208	0.32	0.17	20
	B	1.98	193	186	24.37	25.3	23	208	191	0.29	0.83	73
	A	2.38	195	298	24.58	21.6	37	191	204	0.38	0.66	116
2351+456.....	A	0.22	321	98	27.38	4.5	144	321	296	0.32	0.26	36
Other PR Sample Objects												
0153+744.....	A	0.49	68	3	26.06	...	...	68	0.00	0.00	...	...
0711+356.....	B	0.50	329	7	26.01	<29	...	329	337	0.00	...	...
	A	6.30	337	41	26.78	<18	...	337	...	0.53	0.86	40
1828+487.....	E	0.09	311	322	26.77	7.4	106	311	319	0.23	0.51	113
	D	0.81	319	124	26.36	5.7	133	319	341	0.52	0.30	161
	C	1.85	333	22	25.61	<31	...	341	331	0.71	0.15	142
	B	4.25	332	32	25.77	24.4	163	331	325	0.53	0.31	149
	A	10.23	328	65	26.08	...	...	325	272	1.56	0.47	120

NOTE.—All luminosities are calculated assuming $h = 0.65$, $q_0 = 0.1$, and a zero cosmological constant. Col. (1): IAU source name. Col. (2): Component name. Col. (3): Distance from core component. Col. (4): Position angle with respect to the core component. Col. (5): Fitted Gaussian flux density. Col. (6): Luminosity. Col. (7): Fractional linear polarization, measured at position of I peak. Col. (8): EVPA, measured at position of I peak. Col. (9): Local jet direction, measured upstream of the component. Col. (10): Local jet direction, measured downstream of the component. Col. (11): FWHM major axis of fitted component. A value of zero denotes a δ-function component. Col. (12): Axial ratio of fitted component. Col. (13): Position angle of component's major axis.

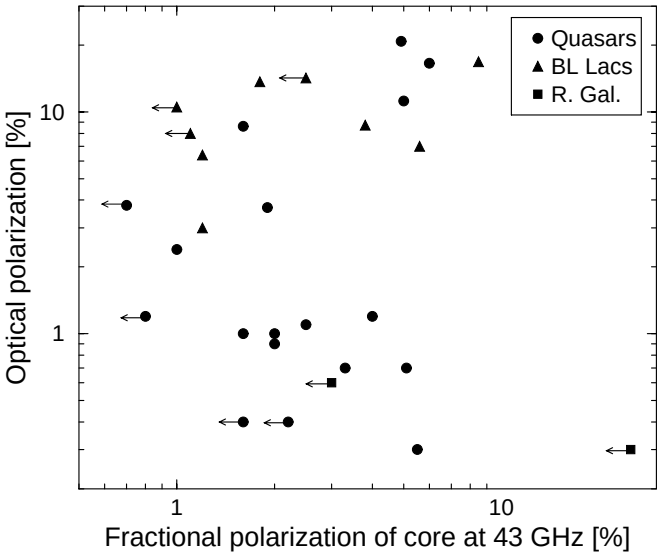

FIG. 36.—Fractional polarization of VLBI core at 43 GHz vs. optical polarization level of the source. Arrows pointing left indicate upper limits on the core polarization.

ization because of increased ordering of the magnetic field. We find evidence for such a scenario in the core components of our sample. Figure 37 shows that as the core polarization increases, the electric vectors tend to align with the jet as predicted. This trend was also found in the polarized *jet* components of another AGN sample at 43 GHz by Lister & Smith (2000). To our knowledge, this marks the first such detection in the core components of AGNs.

The distribution of $|\mathrm{EVPA} - \mathrm{JPA}|$ (top panel of Fig. 37) is somewhat skewed toward low values and has a 5% probability of being drawn from a uniform distribution, according to a K-S test. If strong transverse shocks were dominating the polarization of all the cores, we would expect the observed electric vectors to all lie parallel to the jet, with very few $|\mathrm{EVPA} - \mathrm{JPA}|$ misalignments greater than 10°. Our measured misalignments range up to $\sim 80°$, however. We do not expect the core EVPAs to be significantly affected by Faraday rotation at 43 GHz, since extremely high rotation measures (RMs) of $\gtrsim 25{,}000$ rad m^{-2} would be required to produce a significant effect. Such values are much higher than typical values seen in the

TABLE 5

MEASURED AND DERIVED QUANTITIES FOR THE PEARSON-READHEAD AGN SAMPLE

Symbol	Property
	General Properties
.....	Optical classification (RG, LPRQ, HPQ, BL Lac)
z	Redshift
$\bar{\alpha}_{5-15}$	Time-averaged spectral index between 4.8 and 14.5 GHz
	Variability Properties
V_5	Variability amplitude at 5 GHz
V_{15}	Variability amplitude at 14.5 GHz
$T_{b,\mathrm{var}}$ (K).....	Variability brightness temperature
	Luminosity Properties
$L_{T,5}$ (W Hz^{-1})	Total single-dish luminosity at 5 GHz
$L_{t,43}$ (W Hz^{-1})	Total VLBI luminosity at 43 GHz
$L_{c,5}$ (W Hz^{-1}).....	VLBI core luminosity at 5 GHz
$L_{c,43}$ (W Hz^{-1}).....	VLBI core luminosity at 43 GHz
$L_{C,1.4}$	Kiloparsec-scale (VLA) core luminosity at 1.4 GHz
L_{opt} (W Hz^{-1})	Optical (V-band) luminosity
L_{X} (W Hz^{-1})	X-ray luminosity at 1 keV
	Jet Properties
R.....	Ratio of core to remaining VLBI flux density at 43 GHz
F_c	Ratio of VLBI core to remaining total flux density at 5 GHz
N_{bend} (deg)	Number of significant bends ($>10°$) within 100 h^{-1} projected pc of the core.
Σ_{bend} (deg)	Sum of significant bend angles within 100 h^{-1} projected pc of the core
β_{app}	Fastest measured component speed in jet in units of c
L_{cpt} (W Hz $^{-1}$)	Luminosity of jet component at 43 GHz
d_{cpt} (pc).....	Projected distance of jet component from core
	Polarization Properties
m_{cpt} (%)	Linear polarization of jet component at 43 GHz
$m_{c,43}$ (%)	Linear polarization of VLBI core at 43 GHz
$m_{t,43}$ (%)	Total VLBI linear polarization of source at 43 GHz
m_{opt} (%)	Optical V-band linear polarization
EVPA (deg).....	Electric vector position angle at 43 GHz
$\lvert \mathrm{EVPA}_{\mathrm{core}} - \mathrm{JPA} \rvert$ (deg).....	Offset of core EVPA from innermost jet direction
$\lvert \mathrm{EVPA}_{\mathrm{cpt}} - \mathrm{JPA}_{\mathrm{in}} \rvert$ (deg)	Offset of component EVPA from upstream jet direction
$\lvert \mathrm{EVPA}_{\mathrm{cpt}} - \mathrm{JPA}_{\mathrm{out}} \rvert$ (deg).....	Offset of component EVPA from downstream jet direction

nuclear regions of quasars ($\sim$2000 rad m^{-2}; Taylor 2000). It is possible that the limited resolution of our images may have introduced errors in the measured $|\mathrm{EVPA} - \mathrm{JPA}|$ values because of small-scale jet bending near the core or the blending of unresolved components at the base of the jet. Alternatively, it may be the case that the inner jets of some sources contain only weak shocks that lie at oblique angles to the flow. Data from future high-frequency space-VLBI missions should help us to distinguish between these possibilities.

4.6. *Jet Polarization Properties*

The modest dynamic range of our snapshot maps does not permit an overly detailed analysis of the faint steep-spectrum jet emission from our sample objects. In particular, the lowest fractional polarization that we detected in any jet was approximately 2%. The properties of the jet components in our sample are tabulated in Table 4.

Despite these limitations, we have confirmed an important trend of increasing fractional polarization with distance down the jet, found by Cawthorne et al. (1993; hereafter CWRG) for the PR sample at 5 GHz and by Lister & Smith (2000) for a different AGN sample at 43 GHz. In Figure 38, we plot fractional polarization versus distance for the jet components (excluding the cores) in our sample. Those components with polarized flux density greater than 5 times the rms noise level of the P image are represented by the solid symbols in Figure 38, while the open symbols represent upper limits. We discuss the rising trend in this figure further in § 5.

We have also compared the EVPA values of the jet components with the local jet direction for our sample. Since many of our sources undergo bends at the position of polarized components, we define the local direction in two ways: $\mathrm{JPA_{in}}$ as the position angle of the jet ridge line upstream of the component and $\mathrm{JPA_{out}}$ as the jet position angle downstream. In those cases in which the ridge line is impossible to trace in the image because of low signal-to-noise, we use the angle to the nearest up- or downstream component. In the top panel of Figure 39, we plot the distribution of $|\mathrm{EVPA} - \mathrm{JPA_{in}}|$ for the polarized jet components (excluding the cores) in the FS-PR sample. The distribution of $|\mathrm{EVPA} - \mathrm{JPA_{out}}|$ is shown in the bottom panel. Both distributions are peaked at zero, with the

TABLE 6

CORRELATIONS INVOLVING VLBI PROPERTIES OF THE FS-PR SAMPLE

Property (1)	Property (2)	N (3)	τ (4)	P (%) (5)	τ_z (6)	P_z (%) (7)
$m_{t,43}$	$\bar{\alpha}_{5-15}$	30	0.425	8.79×10^{-2}	0.429	2.97×10^{-4}
R	$m_{\rm opt}$	29	0.429	1.09×10^{-1}	0.444	3.15×10^{-3}
$m_{c,43}$	$m_{t,43}$	31	0.445	4.58×10^{-3}	0.447	4.19×10^{-3}
$m_{c,43}$	$\bar{\alpha}_{5-15}$	30	0.338	3.26×10^{-1}	0.346	4.64×10^{-3}
$m_{c,43}$	$\lvert {\rm EVPA}_{\rm core} - {\rm JPA} \rvert$	21	−0.452	4.04×10^{-1}	−0.459	7.65×10^{-3}
R	V_5	30	0.358	5.47×10^{-1}	0.367	8.27×10^{-2}
$m_{t,43}$	V_{15}	30	0.329	1.02	0.330	1.50×10^{-1}
$N_{\rm bend}$	$\beta_{\rm app}$	20	0.445	6.13×10^{-1}	0.371	6.21×10^{-1}
R	$T_{b,\rm var}$	19	0.427	1.07	0.457	7.22×10^{-1}
R	F_c	24	0.388	7.84×10^{-1}	0.388	7.63×10^{-1}
$N_{\rm bend}$	$L_{\rm X}$	26	0.359	1.01	0.204	1.31
$\Sigma_{\rm bend}$	$\beta_{\rm app}$	20	0.353	2.96	0.312	2.79
Luminosity-Luminosity Correlations						
$L_{c,43}$	$L_{c,5}$	24	0.795	5.27×10^{-6}	0.584	5.55×10^{-2}
$L_{t,43}$	$L_{C,1.4}$	29	0.783	2.45×10^{-7}	0.562	9.87×10^{-2}
$L_{t,43}$	$L_{\rm X}$	25	0.773	6.02×10^{-6}	0.553	1.60×10^{-1}
$L_{t,43}$	$L_{T,5}$	30	0.798	5.98×10^{-8}	0.585	1.69×10^{-1}
$L_{c,43}$	$L_{t,43}$	31	0.784	5.89×10^{-8}	0.589	2.16×10^{-1}
$L_{c,43}$	$L_{\rm X}$	25	0.725	3.84×10^{-5}	0.413	6.08×10^{-1}
$L_{t,43}$	$L_{c,5}$	24	0.674	3.96×10^{-4}	0.324	1.25
$L_{c,43}$	$L_{\rm opt}$	31	0.590	3.16×10^{-4}	0.326	1.29
Correlations with Redshift						
$L_{T,5}$	z	30	0.779	1.47×10^{-7}	...	...
$L_{C,1.4}$	z	30	0.773	1.96×10^{-7}	...	...
$L_{c,43}$	z	31	0.706	2.39×10^{-6}	...	...
$L_{t,43}$	z	31	0.673	1.04×10^{-5}	...	...
$L_{\rm X}$	z	26	0.717	2.81×10^{-5}	...	...
$L_{c,5}$	z	24	0.746	3.23×10^{-5}	...	...
$L_{\rm opt}$	z	32	0.568	4.86×10^{-4}	...	...
$T_{b,\rm var}$	z	20	0.589	2.79×10^{-2}	...	...
Correlations Likely Due to Redshift Bias						
$L_{t,43}$	$L_{\rm opt}$	31	0.539	2.02×10^{-3}	0.260	2.15
$L_{c,43}$	$L_{T,5}$	30	0.723	2.04×10^{-6}	0.391	3.19
$L_{\rm opt}$	$\beta_{\rm app}$	20	0.379	1.95×10^{-1}	0.268	4.40
$L_{c,43}$	$T_{b,\rm var}$	19	0.591	4.10×10^{-2}	0.237	5.20
$L_{c,43}$	$L_{C,1.4}$	29	0.718	4.62×10^{-6}	0.370	5.68
$L_{\rm opt}$	$N_{\rm bend}$	32	0.305	1.42	0.199	7.83
$L_{C,1.4}$	$N_{\rm bend}$	30	0.336	9.02×10^{-1}	0.187	8.08

NOTE.—Cols. (1): and (2): Source property (see Table 5 for symbol definitions). Col. (3): Number of data pairs. Col. (4): Kendall's τ coefficient. Col. (5): Probability of correlation arising by chance. Col. (6): Kendall's τ coefficient, with redshift partialed out. Col. (7): Probability of correlation arising by chance, with redshift partialed out.

majority of components having EVPAs aligned to within 40° of the local jet direction.

This result contrasts dramatically with that of Lister, Marscher, & Gear (1998), who found a uniform distribution of $|{\rm EVPA} - {\rm JPA}|$ for a collection of quasars and BL Lac objects that had been observed at 22 GHz and higher at that time. Their sample did not have well-defined selection criteria, however, and may have suffered from unknown observational biases.

A family of purely *transverse* (i.e., nonoblique) shocks cannot reproduce our data, since their electric vectors are always parallel to the jet, irrespective of beaming and orientation effects (Cawthorne & Cobb 1990). CWRG have suggested that quasar jets contain a strong underlying longitudinal component to their magnetic field that increases with distance down the jet. At the sites of shocks, the longitudinal and transverse fields are superimposed on one another, causing a decrease in the observed polarization. At some distance down the jet, the underlying longitudinal field becomes strong enough to dominate the observed polarization and flip the electric vectors perpendicular to the jet axis. In order to account for the intermediate values of $|{\rm EVPA} - {\rm JPA}|$ in Figure 39 that lie between these two extremes, some other mechanism is required.

Lister et al. (1998) examined the predicted distribution of $|{\rm EVPA} - {\rm JPA}|$ for two possible scenarios: one in which the polarized emission originates in moving, oblique shocks, and the other in which the polarized components are simply enhanced jet regions with fixed magnetic field

TABLE 7

TWO-SAMPLE TESTS FOR VARIOUS SUBCLASSES OF THE FS-PR SAMPLE

Source Property (1)	Symbol (2)	QSO vs. BL Lac Objects (%) (3)	HPQ vs. BL Lac Objects (%) (4)
General Properties			
Redshift	z	0.07*	1.87*
Total VLBI luminosity	$L_{t,43}$	0.07*	0.60*
Total fractional VLBI polarization	$m_{t,43}$	48.65	35.18
VLBI Core Properties			
Luminosity	$L_{c,43}$	0.11*	0.48*
Core dominance	R	54.96	98.21
Fractional polarization	$m_{c,43}$	74.55	29.91
EVPA offset from innermost jet direction	$\lvert \mathrm{EVPA}_{\mathrm{core}} - \mathrm{JPA} \rvert$	86.66	99.38
Jet Properties			
Component luminosity	L_{cpt}	0.07*	0.06*
Component fractional polarization	m_{cpt}	2.96	21.86
Component EVPA offset from upstream jet direction	$\lvert \mathrm{EVPA}_{\mathrm{cpt}} - \mathrm{JPA}_{\mathrm{in}} \rvert$	16.47	37.30
Component EVPA offset from downstream jet direction	$\lvert \mathrm{EVPA}_{\mathrm{cpt}} - \mathrm{JPA}_{\mathrm{out}} \rvert$	1.12*	2.52
Component distance from core	d_{cpt}	0.20*	2.97
Number of jet bends	N_{bend}	53.38	60.30
Sum of bend angles	Σ_{bend}	87.19	60.30
Maximum apparent speed	β_{app}	71.35	44.279

NOTE.—All values represent the probability that the subsamples were drawn from the same population, based on the source property in question. The asterisks (*) denote values less than 2%, which are considered statistically significant. Col. (1): Source property. Col. (2): Symbol. Col. (3): All quasars vs. BL Lac objects. Col. (4): High optical polarization quasars vs. BL Lac objects.

configurations that are drawn from a random orientation distribution. In the case of oblique shocks, they found that the distribution of $|\mathrm{EVPA} - \mathrm{JPA}|$ should be highly peaked at zero and taper off sharply at high $|\mathrm{EVPA} - \mathrm{JPA}|$ values. The nonoblique model also predicts a peak near zero, but its distribution is expected to be flatter and more uniform over the range $5^\circ \lesssim |\mathrm{EVPA} - \mathrm{JPA}| < 90^\circ$.

The distribution of $|\mathrm{EVPA}_{\mathrm{in}} - \mathrm{JPA}|$ in the top panel in Figure 39 is similar in shape to the oblique shock model prediction of Lister et al. (1998) for jets with upstream Lorentz factors equal to 5. There still remain too many uncertainties in the parameters of their model to permit detailed fitting to our data, however. These include the

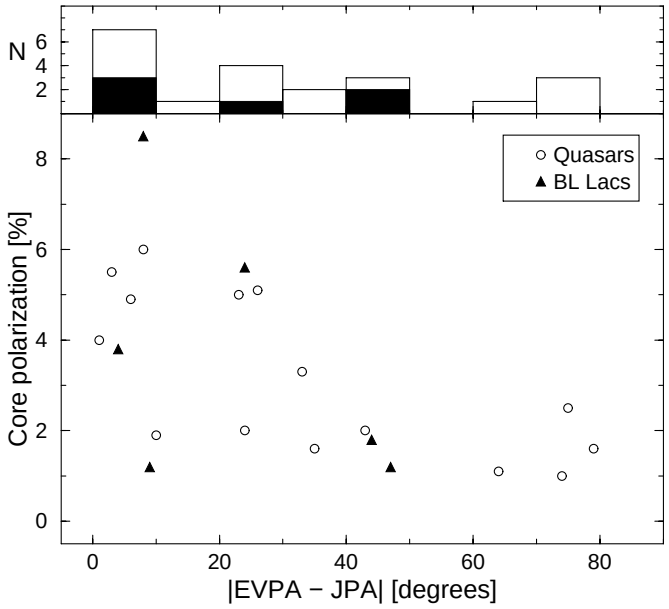

FIG. 37.—Fractional polarization of VLBI core components at 43 GHz plotted against core EVPA offsets with respect to the innermost jet direction. The inferred magnetic fields of cores located toward the left-hand side of the plot are oriented perpendicular to the jet axis.

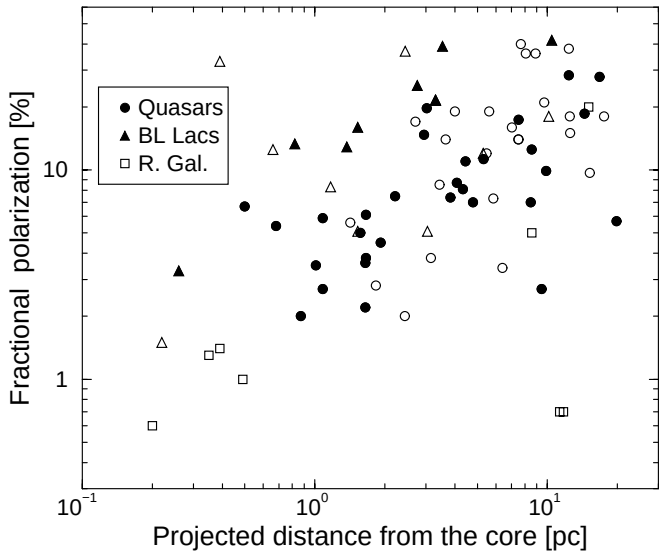

FIG. 38.—Log-log plot of fractional polarization vs. projected distance from the core for jet components in the FS-PR sample. The solid symbols indicate components with detected polarization and the open symbols represent upper limits only.

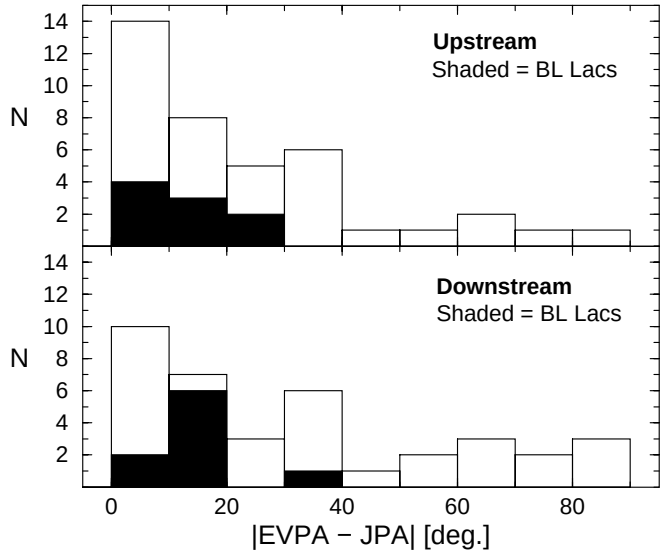

FIG. 39.—*Top*: Distribution of EVPA offset with respect to the local upstream jet direction for polarized jet components (excluding cores) in the FS-PR sample, with BL Lac components shaded. *Bottom*: EVPA offset distribution using downstream position angles.

intrinsic distributions of shock obliqueness, shock speed, viewing angle, and upstream jet speed, upon which there are currently few observational constraints.

There are also uncertainties regarding the true JPAs near the locations of polarized jet components. For example, if we instead compare the component EVPAs with the downstream JPAs (bottom panel of Fig. 39), we cannot completely rule out the nonoblique scenario of Lister et al. (1998). Higher resolution polarization images will be helpful in addressing this issue.

4.7. *Jet Bending*

The combination of previous space-VLBI images of the FS-PR sample at 5 GHz (Lister et al. 2001b) with our high-resolution 43 GHz images has enabled us to trace the parsec-scale morphologies of these sources with unprecedented detail. The majority of jets in the FS-PR sample appear distorted by projection effects, since they are likely viewed nearly end-on. Any slight bends in the jet axis can be greatly amplified, causing apparent bends of 90° or more in some cases. For example, the jet of 1739+522 displays a rotation of nearly 270° in its apparent flow direction in the space of only a few milliarcseconds (see Fig. 23 and additional images in Lister et al. 2001a).

We use two measures to quantify the degree of bending in our sample, which we tabulate in Table 1. We measure both the number of significant bends and their angular sum out to $\sim 100\ h^{-1}$ pc from the core, using a combination of our 43 GHz images, the 5 GHz ground and space-VLBI images from Lister et al. (2001a), and other VLBI images in the literature. We define a significant bend as any change in direction of the jet greater than $\sim 10°$. In order to reduce possible cosmological bias, prior to our measurements we convolved the lower redshift sources with a larger beam in order to simulate the effects of poorer resolution at the median redshift of the sample ($z \simeq 1$). We did not make any corrections for $(1 + z)^4$ surface brightness dimming in the VLBI images. This may cause the number of bends to be overestimated in low-redshift sources, since more of their jets should be visible at a given image sensitivity level. We find no significant difference in the bending quantities of low ($z < 1$) and high ($z > 1$) redshift sources, however. We also find no difference in the bending properties of quasars versus BL Lac objects, even though the latter are located at significantly closer cosmological distances. We attribute this to the fact that most bends tend to occur in the brightest part of the jet, near the core where the signal-to-noise ratio in the VLBI images is high.

4.7.1. *Correlations with Apparent Speed*

We have compared the bending statistics of the jets in our sample with their maximum apparent speeds as tabulated in Lister et al. (2001b), and find that, in general, the straighter jets in the FS-PR sample tend to have slower jet speeds. This is apparent in Figure 40, in which we plot the number of significant bends against $\beta_{\rm app}$. Our Kendall's τ test shows that these quantities are correlated at the 99.39% confidence level. A similar test of $\beta_{\rm app}$ versus the angular sum of the jet bends gives 97.04% confidence for a correlation. We have repeated these tests, adding recent unpublished apparent-velocity data on several FS-PR objects that are part of the VLBA 2 cm survey (K. I. Kellermann 2001, private communication), and find that the confidence levels increase to 99.98% and 99.81%, respectively.

It is not clear whether these trends may merely be due to orientation effects that generally cause jets seen more nearly end-on to have larger apparent bends and faster superluminal speeds. Lister et al. (2001b) did not find apparent jet

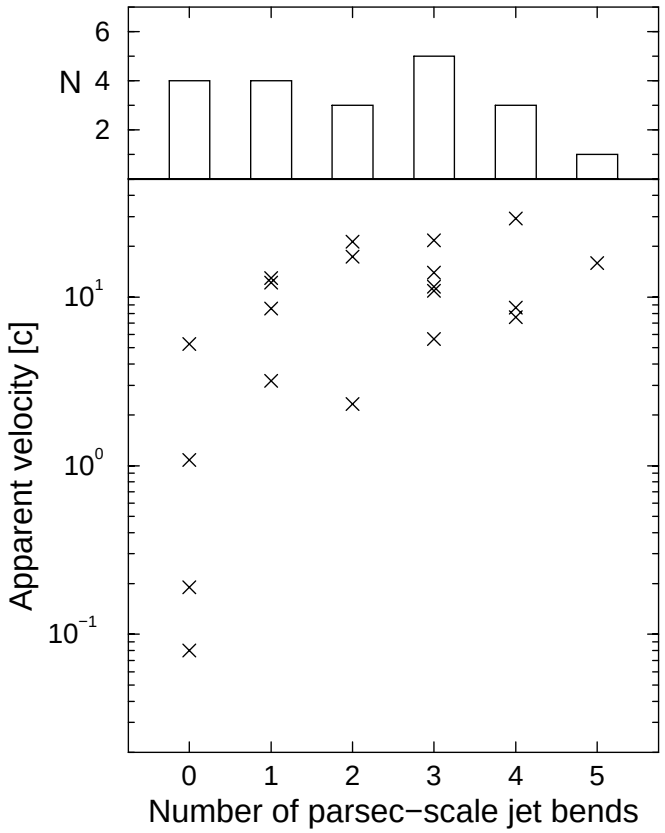

FIG. 40.—Maximum measured apparent jet velocity (in units of *c*) vs. number of significant jet bends (greater than 10°) out to $100\ h^{-1}$ pc from the core.

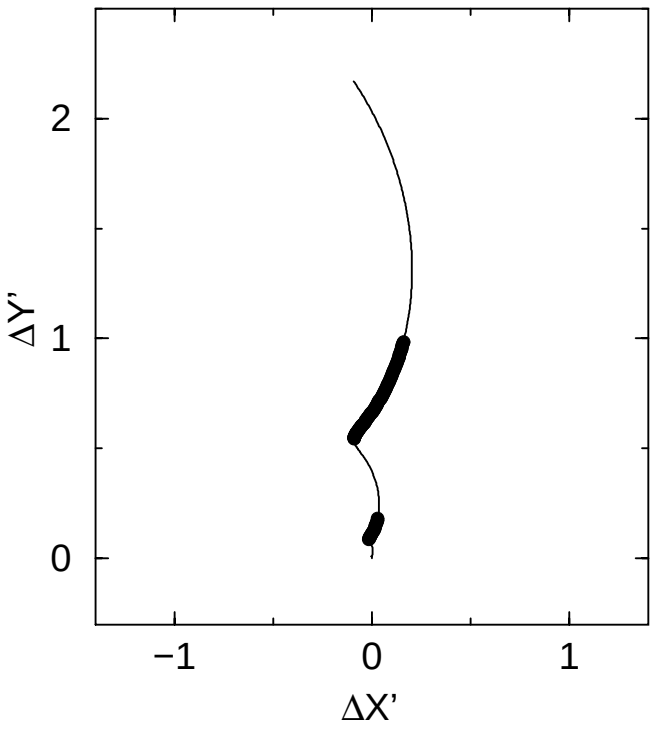

FIG. 41.—Projection of a damped helical jet onto the sky plane for an observer located at a viewing angle of 6° from the helix axis. The regions marked in bold subtend a viewing angle of less than 5°.5 to the observer, and will be significantly Doppler boosted if the bulk flow follows the streamlines and is relativistic. The position angle of the jet is similar in both boosted regions, which is reminiscent of the morphology seen in many of the jets in the FS-PR sample.

speed to be well correlated with jet orientation for the FS-PR sample, however. They attributed this to (1) the narrow predicted range of jet viewing angle for the sample and (2) the likelihood that some sources are viewed inside the critical angle at which apparent velocity is maximized. It is not obvious what physical mechanism could lead to a connection between jet speed and bending. Current theory suggests that jet bends can arise from Kelvin-Helmholtz instabilities that are driven by an external periodic process (e.g., Hardee 1984). Although the evolution of these instabilities is highly dependent on the jet Mach number, it is not clear how the latter quantity is related to the observed VLBI component speeds. More theoretical work is needed to determine how jet speed influences the observed polarization of shocked relativistic jets with intrinsic bends. Detailed three-dimensional magnetohydrodynamical computer simulations should be extremely useful in this regard.

4.7.2. *Bending Morphology*

A large fraction of the jets in the FS-PR sample exhibit a peculiar morphology in which the jet starts out with a particular flow direction, undergoes a bend, and then resumes with nearly exactly the original flow direction. Nearly half of the sources (16 of 35) that we observed at 43 GHz display this "bend and realign" (BAR) morphology, which we indicate in column (11) of Table 1. A good example in our survey can be found in the jet of 1828+487 (Fig. 28), where the position angle between components D and E is very similar to that between A and B, despite a large bend in between these regions. Our two-sample tests do not reveal any strong differences in the overall properties of the BAR versus non-BAR sources in our sample.

The BAR morphology is highly reminiscent of a jet in which the streamlines follow a low-pitch helical pattern, once relativistic beaming effects have been taken into account. Gómez, Alberdi, & Marcaide (1994) have demonstrated that the emission is maximized in jet regions that lie at small angles to the line of sight. We illustrate this in Figure 41, in which the thin line shows the projection of a damped low-pitch helix onto the sky plane (denoted by primes). The axis of the helix lies along the $\hat{z}$-direction in a right-handed coordinate system. The observer is located at a viewing angle of 6° from the $\hat{z}$-axis, and an azimuth direction of 45° from the $\hat{y}$-$\hat{z}$–plane, measured counterclockwise looking down the $+\hat{z}$-axis toward the origin. The helix itself has a half-opening angle of 1° and an increasing wavelength of the form $\lambda = \lambda_0 z^{\epsilon}$, where we have chosen $\lambda_0 = 0.2$ and $\epsilon = 0.3$ in arbitrary units. The regions marked in bold have smaller viewing angles than the rest of the jet, and thus appear much brighter and more beamed. In VLBI images of limited sensitivity, it is possible that these may be the only jet regions that are detected.

We have chosen this particular model merely to illustrate how beaming and orientation effects can conspire to produce BAR morphologies in AGN jets. We note that our model assumes that the bulk motions of the jet plasma follow helical streamlines and are not merely ballistic. Evidence for this can be found in several sources (0859+470, 1641+399, 1642+390, 1803+784, and 2200+420) in which the polarization vectors tend to follow changes in the jet ridge line direction.

5. COMPARISON OF BL LAC OBJECT AND QUASAR POLARIZATION PROPERTIES

A major unresolved issue in AGN research is the relation of high optical polarization quasars to their weak-lined cousins, the BL Lac objects. The separation of these two classes is still a matter of some debate, since the original classification criterion for BL Lac objects (strongest rest-frame emission line width narrower than 5 Å; e.g., Stickel et al. 1991) does not appear to reflect any natural division in the observed line-width distribution of blazars (Scarpa & Falomo 1997). A further complication arises in that the emission line widths of many blazars (including BL Lac itself; Vermeulen et al. 1995) are known to vary with time. Nevertheless, several studies have shown marked differences in the properties of broad- and narrow-lined blazars. These include their spectral properties in the sub-mm (Gear et al. 1994) and X-ray (Padovani 1992) bands and their jet polarization characteristics on parsec scales (CWRG).

CWRG obtained 5 GHz VLBI polarization data on 24 sources in the PR sample, 20 of which are members of the FS-PR sample. They found that the overall jet EVPAs of BL Lac objects tended to be much more aligned with the jet than those of quasars. Compared to our 43 GHz observations, their data were more sensitive to weakly polarized emission farther down the jet, but had significantly poorer spatial resolution and were more influenced by Faraday rotation and depolarization effects. Our data are more sensitive to polarization structure closer to the base of the jet. In this section we compare the 43 GHz VLBI polarization properties of the BL Lac objects and quasars in the FS-PR sample with those obtained by CWRG at 5 GHz. Our BL

Lac classifications are based on the catalog of Padovani & Giommi (1995) and are identical to those of CWRG.

5.1. *Core Components*

CWRG found that at 5 GHz, the VLBI core components of quasars tended to have smaller fractional polarizations than those of BL Lac objects. The $|\mathrm{EVPA}_{\mathrm{core}} - \mathrm{JPA}|$ distributions of both classes were randomly distributed, indicating no preferred orientation of the core magnetic field with respect to the jet. We find a similar result at 43 GHz regarding the core EVPAs (see Fig. 37), but find no significant differences in the core polarization levels of the two classes (top panel of Fig. 34). It is possible that CWRG observed a blend of polarization from components located near the core. This may have reduced the observed polarization of the quasar cores, which are generally located at larger cosmological distances than the BL Lac objects. Higher resolution mm or space-VLBI observations are required to determine whether this is also the case for our 43 GHz observations.

5.2. *Jet Components*

CWRG also found significant differences in the magnetic field properties of BL Lac objects and quasar jets. They showed that BL Lac objects tend to have electric polarization vectors that line up parallel to the jet, while quasars have predominantly perpendicular EVPA orientations. We note that CWRG used a vector-averaged EVPA for the jet and compared it with the position angle of the component with the largest flux density. This method is not appropriate for our data because of the large number of small-scale jet bends present in many sources. We have instead plotted the distribution for all polarized components, compared with the local upstream and downstream jet directions (Fig. 39, top and bottom panels, respectively).

There do appear to be differences in the $|\mathrm{EVPA} - \mathrm{JPA}|$ distributions for BL Lac objects and quasars at 43 GHz, but not as strong a level as reported by CWRG. A K-S test on the BL Lac and quasar distributions in the bottom panel of Figure 39 shows that they differ at the 98.88% confidence level, while in the top panel, the confidence level is only 83.53%. These lower confidence levels are a result of a much stronger tendency for quasar jets to have electric vectors aligned with the jet at 43 GHz than at lower frequencies.

We confirm CWRG's finding that BL Lac jet EVPAs are preferentially aligned with the local jet direction. There are no BL Lac jet components with $|\mathrm{EVPA} - \mathrm{JPA}| > 40°$, irrespective of whether we use the upstream or downstream JPAs. If the intrinsic distribution of $|\mathrm{EVPA} - \mathrm{JPA}|$ were in fact uniform between 0° and 90°, the binomial probability of finding all nine BL Lac components in the first four bins of Figure 39 by chance is only $(4/9)^9 = 0.068\%$.

The connection between jet magnetic field properties and optical line emission is also apparent in Figure 42, in which we plot the EVPA offset of each jet component against the rest-frame equivalent width of the broadest permitted line in the source's optical spectrum. The latter data were tabulated by Lawrence et al. (1996) and Lister et al. (2001b). It is evident that all the components with $|\mathrm{EVPA} - \mathrm{JPA}| > 40°$ are found in sources having emission lines broader than ~ 8 Å.

Despite finding apparent differences in the electric field orientation of BL Lac and quasar jets, CWRG did not find any significant differences in their degree of polarization. A K-S test on our 43 GHz data (Fig. 43) gives a 97.04% probability that the m_{cpt} distributions of the two classes are different, which is slightly below our cutoff level of 98%, at which we call a correlation significant. Evidence of a difference in 43 GHz fractional polarization levels can, however,

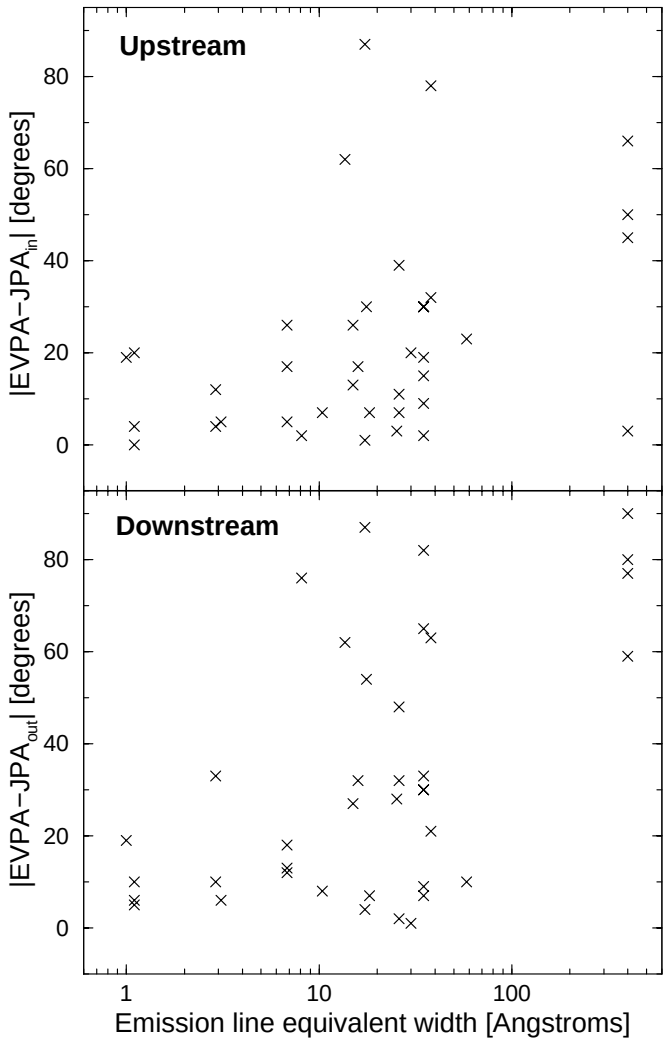

FIG. 42.—*Top*: EVPA offset of polarized jet components with respect to the upstream jet direction, plotted against the rest-frame equivalent width of the broadest permitted line in the source. *Bottom*: Same plot using downstream jet directions.

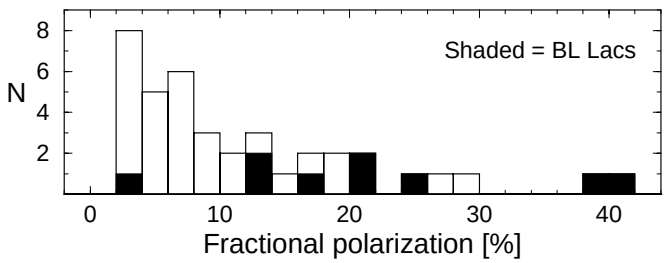

FIG. 43.—Distribution of 43 GHz fractional polarization for jet components with detected polarized emission, with those of BL Lac objects shaded.

be found in the plot of m_{cpt} versus projected distance from the core (Fig. 38). This plot shows that *at a given projected distance from the core*, the fractional polarizations of BL Lac components are generally higher than those of quasars.

5.3. *Longitudinal Magnetic Field Model*

CWRG interpreted their polarization findings at 5 GHz in terms of a model that incorporates a longitudinal magnetic field component present in the jets of quasars, but not in those of BL Lac objects. They claimed that the underlying jet polarization in quasars is very strong and increases down the jet because of shear with the external medium. The observational signatures of this model are a general tendency in quasars for the fractional polarization to increase and the EVPAs to become more perpendicular to the jet axis as you move downstream from the core.

Although the longitudinal field model does appear valid at large distances downstream, several difficulties arise when we attempt to apply it to regions closer to the core. First, we find that at 43 GHz, quasars in fact contain many polarized components with electric vectors *parallel* to the jet, suggesting that shocks dominate any underlying longitudinal field in these regions. Second, we find no tendency for the EVPAs to become more perpendicular to the jet with increasing distance from the core. Indeed, the four quasar components with perpendicular EVPA alignments (greater than 60° from the upstream jet direction) are all located within 2 pc (projected) of the core, and not far downstream. It would appear likely then, that in the jet regions within several milliarcseconds of the core, the longitudinal shear component of the magnetic field has not yet fully developed. In this case, the trend of increasing polarization may instead result from some other mechanism, such as an increase in shock strength or viewing angle with core distance. Lister & Smith (2000) point out that a jet that is bending away from the observer can create an increasing trend of fractional polarization with distance, given the right geometry. Since apparent velocities are also dependent on viewing angle, it should be possible to distinguish between an increase in shock strength versus an increase in viewing angle by monitoring the superluminal speeds and polarization properties of components as they move down the jet.

In summary, we find evidence for fundamental differences in the inner jet properties of BL Lac objects and quasars that need to be investigated in more detail using higher sensitivity images taken at multiple epochs. Such data can yield good constraints on the strengths and viewing angles of relativistic shocks (e.g., Wardle et al. 1994) and would clarify considerably our observational picture of the magnetic field structures in AGN jets.

6. CONCLUSIONS

We have carried out the first 43 GHz VLBI polarization survey of a complete sample of active galactic nuclei at a resolution of ~ 0.2 mas, making this the highest resolution imaging survey of a complete AGN sample made to date. Our sample consists of a flat-spectrum subset of the well-known Pearson-Readhead (FS-PR) survey , which has been thoroughly studied at a variety of wavelengths and resolution levels. We have investigated the jet magnetic field properties of these objects on parsec-scales close to the central engine. The main results of our study are:

1. The morphologies of bright, flat-spectrum AGNs at 43 GHz generally consist of a bright core component located at the base of a faint one-sided jet. On average, the core component accounts for $\sim 60\%$ of the total VLBI flux at this frequency. Its luminosity is well correlated with numerous other luminosity parameters, including the total source luminosity in soft X-rays, in the optical, and at 5 GHz.
2. The ratio R of VLBI core-to-remaining VLBI flux is well correlated with several statistical indicators of relativistic beaming, namely optical polarization, 5 GHz radio variability amplitude, and variability brightness temperature.
3. The linear polarizations of the core components in the FS-PR sample range up to $\sim 9\%$, with typical values of $\sim 1.5\%$. Although the jets generally show higher *fractional* polarization levels than the cores, the bulk of the polarized emission on parsec-scales comes from the core component. In contrast to previous 5 GHz VLBI measurements, we find the cores of BL Lac objects and quasars to have similar polarization levels at 43 GHz. Also, sources with more highly polarized cores tend to have flatter spectral indices measured between 5 and 15 GHz.
4. There is a tendency for the more highly polarized cores to have electric field vectors that lie preferentially along the jet axis. This behavior is consistent with shocks in the inner jet flow that preferentially compress the perpendicular component of the magnetic field.
5. Among the sources with optical polarizations (m_{opt}) exceeding $\sim 1\%$, there is a positive trend of m_{opt} with 43 GHz core polarization, which suggests a common origin for the emission at these two frequencies. We find no such trend among the lower optically polarized objects.
6. The fractional polarization of jet components tends to increase with projected distance down the jet in a similar manner for both BL Lac objects and quasars. However, at a given distance from the core, the jet components of BL Lac objects are more polarized and have magnetic fields preferentially aligned perpendicular to the jet.
7. The vast majority of polarized components located in the jets of both BL Lac objects and quasars have electric field vectors that lie within 40° of the local jet direction. The distribution of electric vector offsets with respect to the jets in the entire sample is consistent with theoretical predictions for an ensemble of moving oblique shocks.
8. We find that straighter jets tend to have smaller apparent jet speeds than sources that display significant jet bending. Nearly half of the jets in the FS-PR sample display a "bend-and-realign" (BAR) morphology that is a predicted feature of jet plasma streaming relativistically along a helical path. We find support for such streaming motions in several objects whose electric vectors closely follow significant changes in the jet direction.

The author thanks Bob Preston, Glenn Piner, and Steven Tingay for helpful discussions during the planning stages of this project, and Alan Marscher and an anonymous referee for comments on the manuscript. Thanks also go to Harri Teräsranta for providing flux-density data and Tim Cawthorne, Alan Marscher, Svetlana Jorstad, and Ken Kellermann for providing VLBI data in advance of publication.

This research was performed in part at the Jet Propulsion Laboratory, California Institute of Technology, under con-

tract to NASA, and has made use of data from the following sources: the NASA/IPAC Extragalactic Database (NED), which is operated by the Jet Propulsion Laboratory, California Institute of Technology, under contract with the National Aeronautics and Space Administration, and the University of Michigan Radio Astronomy Observatory, which is supported by the National Science Foundation and by funds from the University of Michigan.

REFERENCES

Akritas, M. G., & Siebert, J. 1996, MNRAS, 278, 919
Aller, M. F., Aller, H. D., & Hughes, P. A. 1992, ApJ, 399, 16
Berriman, G., Schmidt, G. D., West, S. C., & Stockman, H. S. 1990, ApJS, 74, 869
Bloom, S. D., Marscher, A. P., Moore, E. M., Gear, W., Teräsranta, H., Valtaoja, E., Aller, H. D., & Aller, M. F. 1999, ApJS, 122, 1
Cawthorne, T. V., & Cobb, W. K. 1990, ApJ, 350, 536
Cawthorne, T. V., Wardle, J. F. C., Roberts, D. H., Gabuzda, D. C., & Brown, L. F. 1993, ApJ, 416, 496 (CWRG)
Dermer, C. D., & Schlickeiser, R. 1993, ApJ, 416, 458
Gabuzda, D. C., Pushkarev, A. B., & Cawthorne, T. V. 2000, MNRAS, 319, 1109
Gear, W. K., et al. 1994, MNRAS, 267, 167
Gehan, E. 1965, Biometrika, 52,203
Gómez, J.-L., Alberdi, A., & Marcaide, J. M. 1994, A&A, 284, 51
Hardee, P. E. 1984, ApJ, 287, 523
Hughes, P. A., Aller, H. D., & Aller, M. F. 1985, ApJ, 298, 301
Impey, C. D., Lawrence, C. R., & Tapia, S. 1991, ApJ, 375, 46
Lähteenmäki, A., & Valtaoja, E. 1999, ApJ, 521, 493
Laing, R. A. 1980, MNRAS, 193, 439
Lavalley, M., Isobe, T., & Feigelson, E. 1992, in ASP Conf. Ser. 25, Astronomical Data Analysis Software and Systems I, ed. D. M. Worrall, C. Biemesderfer, & J. Barnes (San Francisco: ASP), 245
Lawrence, C. R., Zucker, J. R., Readhead, A. C. S., Unwin, S. C., Pearson, T. J., & Xu, W. 1996, ApJS, 107, 541
Lister, M. L., Marscher, A. P., & Gear, W. K. 1998, ApJ, 504, 702
Lister, M. L., & Smith, P. S. 2000, ApJ, 541, 66
Lister, M. L., Tingay, S. J., Murphy, D. W., Piner, B. G., Jones, D. L., & Preston, R. A. 2001a, ApJ, 554, 948
Lister, M. L., Tingay, S. J., & Preston. R. A. 2001b, ApJ, 554, 964
Marscher, A. P., & Gear, W. K. 1985, ApJ, 298, 114
Meier, D. L., Koide, S., & Uchida, Y. 2001, Science, 291, 84
Padovani, P. 1992, MNRAS, 257, 404
Padovani, P., & Giommi, P. 1995, MNRAS, 277, 1477
Pearson, T. J., & Readhead, A. C. S. 1988, ApJ, 328, 114
Pearson, T. J., Shepherd, M. C., Taylor, G. B., & Myers, S. T. 1994, BAAS, 185, 0808
Scarpa, R., & Falomo, R. 1997, A&A, 325, 109
Stickel, M., Fried, J. W., Kuehr, H., Padovani, P., & Urry, C. M. 1991, ApJ, 374, 431
Taylor, G. B. 2000, ApJ, 533, 95
Vermeulen, R. C., Ogle, P. M., Tran, H. D., Browne, I. W. A., Cohen, M. H., Readhead, A. C. S., Taylor, G. B., & Goodrich, R. W. 1995, ApJ, 452, L5
Wardle, J. F. C., Cawthorne, T. V., Roberts, D. H., & Brown, L. F. 1994, ApJ, 437, 122
Wilkinson, P. N., Polatidis, A. G., Readhead, A. C. S., Xu, W., & Pearson, T. J. 1994, ApJ, 432, L87
Wills, B. J., Wills, D., Breger, M., Antonucci, R. R. J., & Barvainis, R. 1992, ApJ, 398, 454